Master's thesis

NTNU
Norwegian University of Science and Technology
Faculty of Information Technology and Electrical Engineering
Department of Electronic Systems

Mithassel, Benedikt Andreas

Low-energy pyroelectric motion detection

Master's thesis in MTELSYS
Supervisor: Dag Roar Hjelme
Co-supervisor: Pål Øyvind Reichelt
July 2023

NTNU
Norwegian University of
Science and Technology

Mithassel, Benedikt Andreas

Low-energy pyroelectric motion detection

Master's thesis in MTELSYS
Supervisor: Dag Roar Hjelme
Co-supervisor: Pål Øyvind Reichelt
July 2023

Norwegian University of Science and Technology
Faculty of Information Technology and Electrical Engineering
Department of Electronic Systems

NTNU
Norwegian University of
Science and Technology

Table of Contents

List of Figures

List of Tables

Glossary

ADC - Analog to Digital Converter. It converts our analog voltage V_{out} to the digital signal S_D
AFE - Analog Front End, all the analog circuitry that comes before the ADC in the signal path.
Centrosymmetric - A symmetry for which there exists an indistinguishable point (-x,-y,-z) for every point (x, y, z)
DC - Direct Current, in the thesis it is also used to refer to the voltage level around which S_D varies.
DT - Disruptive Technologies, the company for which this thesis is written. They create wireless sensors and IoT infrastructure
DT-die - A low-energy integrated circuit created by DT for measuring analog sensors. It contains the ADC and a hardware implementation of the algorithm presented in section 4.
GPIO - General Purpose Input Output, a digital input/output port on the RPi. GPIO ports on the RPi operate at 3.3V.
IoT - Internet of Things, a network of physical objects, such as sensors connected to the internet
JFET - Junction Field Effect Transistor. The particular type of JFET we find in our circuit is assumed to be TF412S.
LTspice - The particular type of Spice simulator used in this thesis
Node sensor - For this thesis, we choose to define the node sensor as the PCB (Printed Circuit Board) that contains the DT-die, a TI (Texas Instruments) microcontroller, and the antenna. The TI microcontroller is necessary both for having the system communicate with the remaining IoT infrastructure and for allowing the RPi to communicate with the DT-die in a test rig.
Peltier element - An element with a hot side and a cold side. It uses electrical energy to transfer heat from the cold side to the hot side. In the test rig introduced in section 7 the hot side is pointed down towards the sensor element and its temperature is regulated.
PIR - Passive InfraRed, a measurement method for motion detection that is based on sensing the infrared radiation emitted by an object.
Prototype sensor - An IoT sensor system containing the node sensor and the AFE for motion detection
Pyroelectric - The property of generating an electrical potential as a response to temperature change
PZT - Lead zirconate titanate, a pyroelectric material which is the main component of the sensor used in the thesis
RPi - Raspberry Pi, a particular single-board computer.
Spice - Simulation Program with Integrated Circuit Emphasis, the general type of simulator used in this thesis
UART - Universal asynchronous receiver-transmitter, a communication protocol that uses a ground connection and two wires for respectively receiving and transmitting data

Abstract

Current motion-sensing systems consume a relatively high amount of power, making them less suited for wireless applications. This thesis proposes an alternate measurement system for passive infrared (PIR) motion detection, that significantly reduces the consumed power. This is done while still maintaining a similar quality of the detections.

The method used for achieving this is to duty cycle the system. In the proposed system we let the sensing element control the charge over a capacitor, which is then measured and emptied. This is opposed to the more standard approach of having it control the current flow through a resistor.

For a measurement of a human passing under a ceiling-mounted sensing device, the proposed system achieves a calculated power consumption as low as 450pW. For comparison current low-energy systems for PIR detection consume about 6μW[12], while a normal PIR sensor generally uses about 250μW.[11]

The quality of the signal from the measurement system is discussed in detail. This discussion involves noise calculations, the creation of a test rig, Spice simulation, and possible signal processing techniques. There is found to be no noticeable loss of performance, even with the improvement in power consumption. Creating the proposed measurement circuit in practice requires the disassembly of an existing sensor element, and this is discussed in some detail.

In the end, a full IoT (Internet of Things) system featuring this measurement system is implemented and described.

Sammendrag

Eksisterende løsninger for bevegelsesdeteksjon har et høyt energikonsum, hvilket gjør dem mindre egnet til IoT (Tingenes internett) applikasjoner. Denne masteroppgaven beskriver en ny alternativ måte å måle signalet, med et betraktelig lavere energiforbruk. Sensorelementet som benyttes er et PIR (Passive InfraRed) element. Det foreslåtte systemet oppnår et energiforbruk beregnet så lavt som 450pW. Til sammenlikning opererer eksisterende lavenergisystemer for PIR-deteksjon med rundt 6μW[12], mens en vanlig pir-sensor typisk bruker rundt 250μW.[11]

Metoden for å oppnå dette lave energiforbruket er å "duty-cycle" systemet. I det foreslåtte systemet kontrollerer PIR-elementet ladningen over en kondensator, som tømmes mellom hver måling. Dette er i motsetning til mer standard målemetoder, som går ut på å la PIR-elementet regulere strømmen gjennom en resistor, og måle spenningen over resistoren.

Denne forbedringen i energiforbruk går i liten grad på bekostning av signalets kvalitet, og det er ingen merkbar forverring i ytelse sammenliknet med eksisterende systemer. Signalets kvalitet blir diskutert i detalj. Dette inkluderer diskusjon rundt støykomponenter i systemet, en test-rigg for repeterbare eksperimenter, Spice-simulering, og metoder for signalbehandling. Å lage det foreslåtte systemet innebærer en dekonstruksjon av eksisterende komponenter, da komponentene som benyttes ikke er å få som hyllevare.

Til slutt blir et fullt IoT bevegelsesdetekssjonssystem som benytter den foreslåtte løsningen implementert og diskutert.

1 Introduction

1.1 Motivation

The goal of this thesis is to explore the degree to which one can reduce the energy consumed by a passive infrared (PIR) pyroelectric sensing system.

Previously this optimization has been of limited interest since these systems are often wired, and thus have access to a sufficient amount of energy. These are systems such as motion-activated light switches and sinks. PIR sensing also finds applications in mapping the amount of activity in spaces, for instance in offices or stores. In these cases, wired installation can be rather expensive and cumbersome, both for wiring the power and the data lines. The requirement that the system must be wired also places limits on where one can deploy the system.

One way to remedy these problems is to employ a wireless system, in which it is possible to acquire the data from the sensors remotely over the internet. Such a sensor would be considered an IoT (Internet of Things) device. The advantages of installation of such a device are evident, it is much easier to simply stick a device to the surface where you want it than having to wire it, especially if wires are not readily available. This is particularly noticeable during the installation of a large number of devices.

Amassing data from multiple motion detectors and obtaining a real-time (and historical) overview of all the sensors in a more convenient way is also a possible advantage of having the data streamed wirelessly to the same platform.

There are existing IoT solutions for PIR sensing. An example of this is the sensor [31] Disruptive Technologies (DT) [22] already uses. DT is the company for which this thesis is written. [1] Their existing PIR sensor has a battery life of up to ten years, and the general approach to achieving such a battery life in PIR devices is to use large batteries.

This means that in a system containing a PIR sensor element, that element constitutes the bottleneck for what sort of batteries one can use and therefore also is the bottleneck for reducing the size. This thesis argues that this does not need to be the case, and that it is possible to reduce the size about an order of magnitude by using a single CR1216 button cell battery [8] and still maintain a lifetime of more than a decade with the same functionality. An advantage of this is that the form factor of the sensor will be more in line with the rest of Disruptive Technologies lineup of sensors [22], which for the most part have a size of 19x19x2.5 mm, thereby making them the world's smallest IoT sensors of their kind.

Batteries are one of the main limiting factors of the total number of IoT node devices in the world today. If one is to have the amount of IoT nodes predicted to exist within the next three years one would, even if one assumes a battery lifetime of ten years, have to change hundreds of millions of batteries daily [27]. Pushing the energy consumption down to the order of magnitude at which the node can harvest a sufficient amount of power to not require a battery is a way to overcome this barrier limiting the amount of IoT nodes.

The thesis proposes a measurement method allowing for a power consumption of 450pW,

[1] The most important contributions from Disruptive technologies are providing the platform on which the prototype presented in section 11 is built, as well as the time and input of my advisor Pål Øyvind Reichelt. More information regarding the contributions of Disruptive Technologies to this thesis may be found in appendix A.3

mainly achieved through duty cycling. An IoT device built upon that measurement method is also presented.

1.2 Outline of thesis

This thesis will first provide relevant background theory in section 2, 3, 4, and 5. Following this, a new method for low-energy motion detection is presented in section 6. The remainder of the thesis is mostly concerned with verifying that the proposed circuit works well. This verification includes the construction of a test rig, modification of the sensor element, Spice simulation, and incorporation of the circuit into a full low-energy IoT (Internet of Things) system. The background theory includes an introduction to pyroelectric physics, typical measurement methods and algorithms for motion detection, and an overview of noise sources.

The important takeaway we will get from section 2, which describes the physics behind pyroelectricity, is what sort of signal motion near the sensor results in and why.

Section 3 will then go on to describe methods typically used for motion detection with pyroelectric elements. Typically a source follower is used to decrease the output impedance of the pyroelectric element, as presented in section 3.1. One might also use a Fresnel lens to better detect small movements, and a differential pair can be used to increase robustness to environmental temperature changes. This is described in section 3.2. Capacitors may also be added to smooth the signal, as described in section 3.3.

Section 4 goes on to describe the algorithm for motion detection. Once we have a signal out of the analog front-end circuitry (AFE) we somehow need to decide whether any motion occurred. Three algorithms of increasing complexity are presented. Simple thresholding, presented in section 4.1 is the simplest and most understandable algorithm, underpinning the other two. Moving thresholding, in which the threshold is dynamic, presented in section 4.2 adds robustness against environmental changes. Finally, batch averaging, which can be more easily implemented in hardware, is presented in section 4.3.

In section 5 we look at the theoretical background for noise, which affects signal quality.

In section 6 a new method for low-energy motion detection is presented. It consists of two seemingly small changes with large implications for energy consumption. The first, and most important, is to duty cycle the system. The second is to switch out the resistor, in the source follower to which the pyroelectric element is connected, with a capacitor. This provides a large degree of control over the amount of charge that flows through the measurement system. Almost all the background theory relevant to typical motion detection methods is still relevant to this new system.

A test rig is presented in section 7. The purpose of this test rig is to control the heat radiated onto the sensor in a way that is equivalent to a human passing the sensor. Having this parameter under control allows for more consistent measurements. An overview of it is presented in 7.1, and then the individual parts are discussed in the following sections. Section 7.2 and 7.3 discuss controlling the irradiation onto the element, and section 7.4 discusses parts responsible for noise reduction. Section 7.5 discusses the radiation from a person passing the sensor in further detail.

Section 8 discusses some practical concerns regarding how one could modify an off-the-shelf sensor to get a sensor element that fits the specifications in this thesis.

Simulation of the system, using LTspice, is presented in section 9. This helps us gain an understanding of the system that is not clouded by the practical measurement considerations in the test rig. The simulation results correspond to what is expected based on the prior discussion.

Empirical findings regarding the signal quality of the system will be discussed in section 10. This ties together a lot of what is presented so far. We measure the circuit presented in section 6 using the test rig presented in 7 and compare it to the simulation from section 9. The measured signal quality will be discussed with regard to the theoretical background presented in section 5. In section 10.6 The performance of the system will be discussed for different parameters of the algorithm presented in section 4.

In section 11 a full IoT system that incorporates the proposed measurement method is presented.

After this, there is some discussion regarding possible future work in section 12, and then the thesis concludes in section 13.

2 Theory of pyroelectric physics

A pyroelectric material generates a voltage as a response to a change in temperature. This can be used for detecting human presence. The idea is that a human moving close to pyroelectric material causes it to heat up since we radiate IR (Infrared radiation). This heating in turn causes the material to generate a potential, which we then measure and register as a motion detection.

Section 2.1 and 2.4 describe why we get the pyroelectric response. Section 2.2 describes an equivalent model for pyroelectric elements, and section 2.3 describes the shape of the pyroelectric current.

2.1 Pyroelectric materials in context

Figure 1 shows that pyroelectrics are a subset of piezoelectrics, which again is a subset of dielectrics. A piezoelectric material creates an electrical response to pressure. A pyroelectric material creates an electrical response to changes in temperature. A ferroelectric is a pyroelectric that has the additional property that applying a strong electrical field to it may change the direction of pyroelectric polarisation, and that direction remains even after the field is removed. The sensor that this thesis concerns itself with, PL-N823-01 is based on PZT (Lead Titanium Zirconium Oxide) and is therefore ferroelectric. [17, p.4] The property of ferroelectricity is not very relevant to the use of this sensor in this thesis, but an advantage of the fact that it is based on PZT is that it may have a large pyroelectric constant, which means that the response to temperature changes is larger.

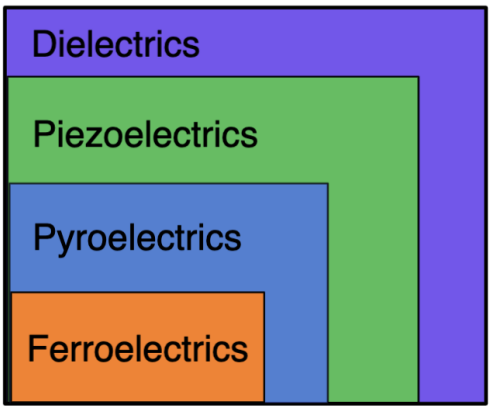

Figure 1: How pyroelectrics fit into the context of different dielectrics. Ferroelectrics are a subset of pyroelectrics which are a subset of piezoelectrics, which again is a subset of dielectrics.

The fact that any pyroelectric also exhibits piezoelectric properties gives rise to the so-called secondary pyroelectric effect. If a material heats up it will expand, and if that material is clamped this will increase the mechanical stress, leading to a piezoelectric response to the heating. In addition to the mechanical boundary condition of being clamped, electrical boundary conditions (applying a field) may contribute to a pyroelectric response in materials that would otherwise have no such response.[18] A material that exhibits pyroelectric properties due to being put under such boundary conditions is called an artificially induced pyroelectric.

Several more phenomena contribute to the polarization (for instance optical polarisation, low inertia polarisation, elastic rotation of connected dipoles and other contributions to permittivity).[18]. However, the phenomenon of pyroelectricity due to mixed covalent-ionic bonds is of special interest, since one finds this kind of bond in PZT. This phenomenon is a primary pyroelectric effect and will be discussed in section 2.4.

2.2 Pyroelectric equivalent models theory

Figure 2 shows an equivalent model for a pyroelectric element. It provides a temperature-dependent current I_p and has a leakage resistance R_p as well as a capacitance C_p. The voltage out of the pyroelectric is V_p.

The capacitance C_p is the actual capacitance of the pyroelectric, not just a theoretical construct. It is given by the material properties and geometry of the element.

As a first approximation, one can consider C_p to be a parallel plate capacitor and find it as

$$C_P = \frac{\epsilon \cdot A_P}{h} \tag{1}$$

where A_p is the area of the pyroelectric, h is its thickness, and ϵ is its permittivity.

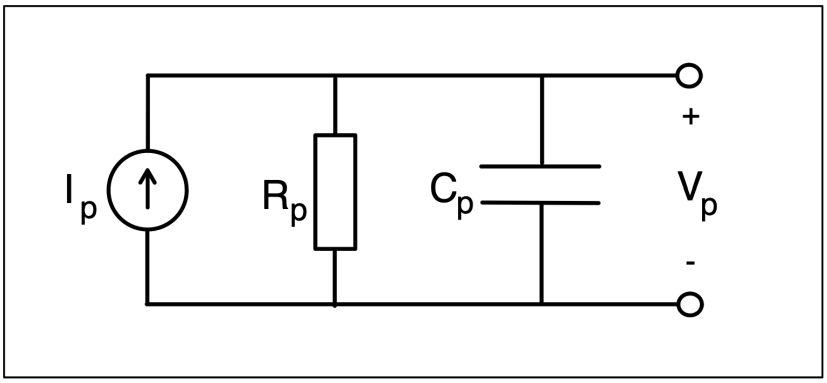

Figure 2: An equivalent model for the pyroelectric element. It provides a temperature-dependent current I_p and has a leakage resistance R_p as well as a capacitance C_p. The voltage out of the pyroelectric is V_p.

For most applications, R_p is so large that it may be ignored, as discussed in [24]. This is shown in figure 3. The model in figure 3 is what will be used for the rest of this thesis.

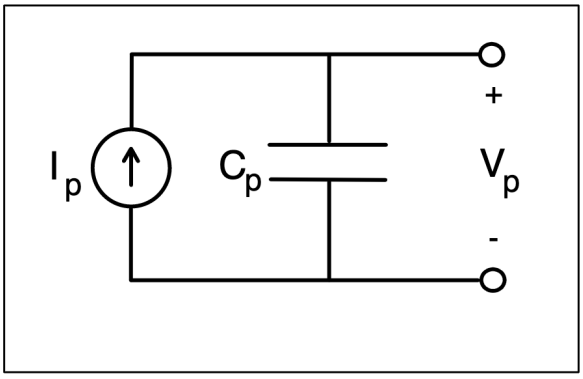

Figure 3: The resistor is so large that in most practical cases it can be ignored. A simpler model that only includes the capacitor and the current source is usually sufficient. It is this model that will be used in this thesis.

2.3 Pyroelectric current

As stated earlier the charge over the pyroelectric is given as $\Delta Q = Ap\Delta T$. The current is how much charge passes a given point over time, so it is natural that the pyroelectric current I_p is given as the derivative of ΔQ

$$I_p = A \cdot p \cdot \frac{\partial T}{\partial t} \tag{2}$$

The heating of the pyroelectric element follows Stefan-Bolzmanns law. This means it has a shape similar to what is shown in figure 4.[2]

[2]The shape in figure 4 is not generated by simulation or measurement, but hand drawn. Figure 4, 11 and 14 are the only graphs for which this is the case.

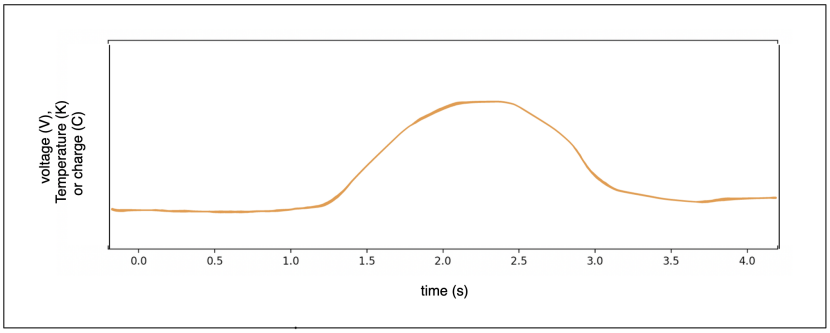

Figure 4: Heating and cooling of a sensor element briefly exposed to a temperature source. This exposure could for instance be from a human passing the sensor element. The heating and cooling are calculated based on Stefann-Bolzmanns law. This shape will also correspond to the shape of V_p. The purpose of this figure is just to convey the shape, and because of this, the y-axis is not numbered.

Since I_p is given as the time derivative of the temperature the shape will be the gradient of the function shown in figure 4. I_p will be integrated by the capacitor C_p to result in V_p. This means V_p has the same shape as the heat signal, since this integration inverts the derivative, as shown below.

$$T = \int \frac{\partial T}{\partial t} dt \propto \int I_p dt \propto V \tag{3}$$

An estimation of the energy radiated onto the element from a human passing it (which causes the temperature increase) is given in section 7.5.

2.4 Mixed covalent-ionic bonds

The pyroelectric effect (unless artificially induced) can only be found in non-centrosymmetric crystals. An intuitive way to understand why this is the case is that temperature is a scalar quantity, and it is to be translated into a polarization which is a vector quantity. In order for there to be a preferred direction of polarization the crystal cannot be completely symmetric in all directions.

The pyroelectric effect also occurs in crystals with mixed ionic-covalent bonds. Such bonds are illustrated in figure 5. Crystals based on mixed ionic-covalent bonds do not need an external field to exhibit pyroelectric properties. [18, p.26]

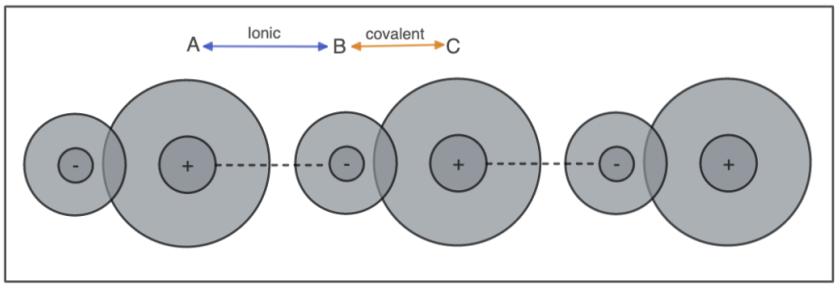

Figure 5: Mixed covalent-ionic bonds. Atoms A and B share an ionic bond, and B and C share a covalent bond. This is a 1-dimensional simplification of a crystal structure, and the pattern of atoms is repeated along the x-axis. The direction of these bonds makes it clear that this crystal structure is not centrosymmetric.

Figure 6 shows a different representation of the same idea as in figure 5. There is an ionic bond between A and B (illustrated as a blue spring) and a covalent bond between B and C (illustrated as an orange spring). These bonds can be modeled as springs, with different spring constants. The spring constant between A and B is called f_1 and the spring constant between B and C is called f_2, and they represent how "stiff" a spring is. The reason the $f_1 \neq f_2$ is that they represent different kinds of bonds.

As the temperature increases the value for f_1 and f_2 change differently, that is, the stiffness of the different springs is unequally affected. This will on average skew atom B either upwards toward A or downwards toward C depending on the temperature. This offset is similar for all the negative ions in the lattice, and on average this can be seen as a charge accumulation on the edge of the element. The pyroelectric element can therefore be modeled as a planar capacitor with a charge that varies as $\Delta Q = Ap\Delta T$. [2] A is the area of the capacitor, and intuitively the total amount of surface charge is proportional to the area of the element. The factor p is the pyroelectric coefficient, which (among other effects) states something about the difference in temperature response between f_1 and f_2. ΔT is a temperature change.

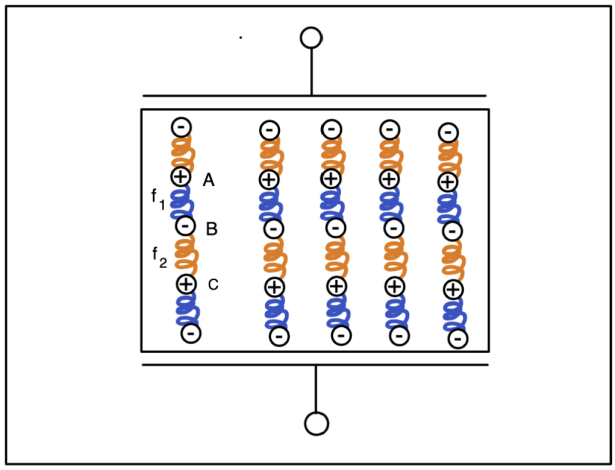

Figure 6: The bonds can be modeled as springs. The colors and naming of atoms in this figure correspond to figure 5. Due to the bonds being different (ionic/covalent) we also have different spring constants $f_1 \neq f_2$. Additionally, the temperature response is different between f_1 and f_2. The abstraction of viewing the element as a system of springs is from [2].

3 Standard circuitry for pyroelectric motion detection

3.1 Source follower

The first stage of PIR detection circuitry generally involves the pyroelectric element connected to a source follower as illustrated in figure 7. The purpose of having the source follower is to decrease the output impedance of the pyroelectric element. Decreasing the output impedance is desirable because then the impact of the impedance of the measurement circuitry on the signal is decreased. For further information about source followers the reader may refer to [7, Chapter 3.3].

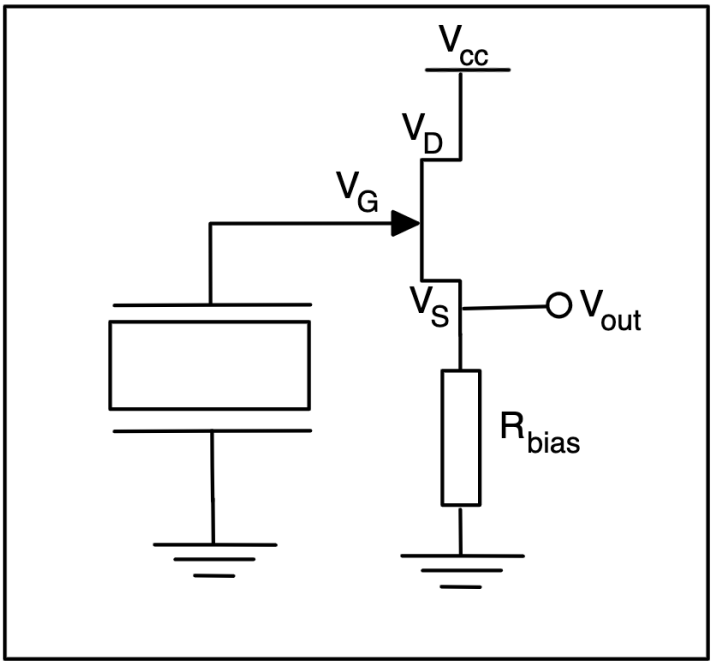

Figure 7: A pyroelectric element and a source follower. The symbol for the pyroelectric element is the box on the left side of the figure. The voltage across the pyroelectric element is applied to the gate of the transistor. The voltage V_{out} follows the voltage applied to the gate.

3.2 Fresnel lens and differential pair

A problem with the way the sensor operates so far is that ΔT only changes when someone moves out of the field of view or into the field of view of the sensor, and as such motion within the field of view of the sensor is not detected. To remedy this one can put a fresnel lens in front of the sensor element. The result of doing this is that the IR-radiation is attenuated as shown in figure 8. This would break up the area into/out of which we detect movement into smaller areas, and thus allows detection of smaller movements. Note that not all fresnel lenses have the property of breaking up the modulation pattern in this way. However, the fresnel lenses used in PIR-sensing typically do.

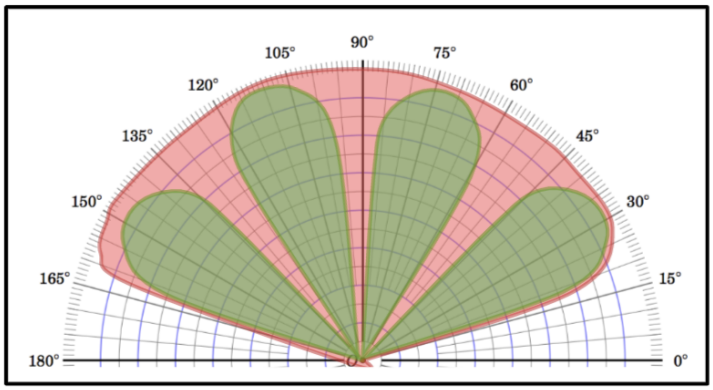

Figure 8: Attenuation from fresnel lens. Instead of the modulation pattern being uniform in the sensor's field of view (illustrated by the red modulation pattern), it is broken up into smaller sections (illustrated by the green lobes of the modulation pattern). The result of this is that we can no longer just see movement into/out of the red lobe, but into and out of the green lobes instead, which means we can detect smaller movements. Note that this is an example for illustration purposes and that the angles are not exact.

Another technique that can be used to improve motion detection is to employ a differential pair of elements biased in opposite directions. This is illustrated in figure 9. Oppositely biased elements provide a level of immunity against changes in ambient temperature. The ambient temperature changes will affect the pyroelectric elements equally, and therefore they cancel each other out. The temperature changes of a moving object, on the other hand, will still result in a signal. This is because the sensor elements are not placed in the exact same location (but rather next to each other), so they do not see the same ΔT. The Fresnel lens is placed close to the pyroelectric elements and ensures that the modulation patterns within the field of view of elements A and B are slightly different.

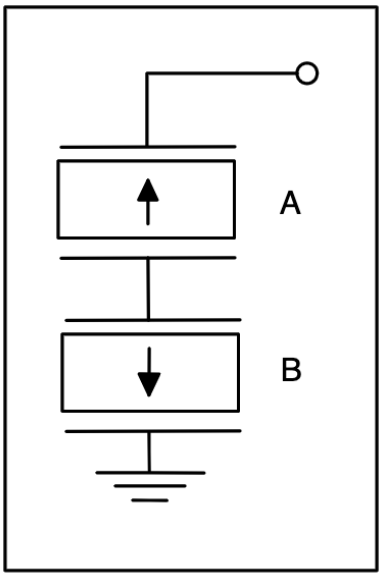

Figure 9: A differential pair of pyroelectric elements. They are biased in such a way that if they were to see the same increase in ΔT element B would set up a positive voltage and element A an equal negative voltage, and as such they would cancel each other out. However due to not being placed in the exact same location they do not see the same ΔT and this difference in temperature between the two pyroelectric elements is a clearer signal than just the ΔT onto a single element.

3.3 Adding capacitors

In order to get the cleanest possible signal one might want to add a capacitor between V_{CC} and ground to have a stable power supply. Adding a capacitor between V_{out} and ground is the same as making a low pass filter out of that capacitor and R_{bias}. Since the actual signal we wish to observe (that of a person moving in front of the sensor) is very slow, it might be advantageous to pass the signal through such a filter.

3.4 Combining the techniques in normal operation

Figure 10 shows a circuit that combines the techniques mentioned so far.

The output of this circuit is V_{out}. [3] V_{CC} is held at a constant voltage. The pyroelectric element (orange box) is composed of two oppositely biased elements as discussed in section 3.2. The transistor and R_{bias} together constitute a source follower, as discussed in section 3.1. The capacitors are for smoothing the signal, as discussed in section 3.3. The purple box corresponds to what one finds on the sensor element PL-N823-01 [17] used for this thesis.

[3] Depending on what AFE we use, V_{out} may have different properties, but it is always the node at which we measure the analog signal.

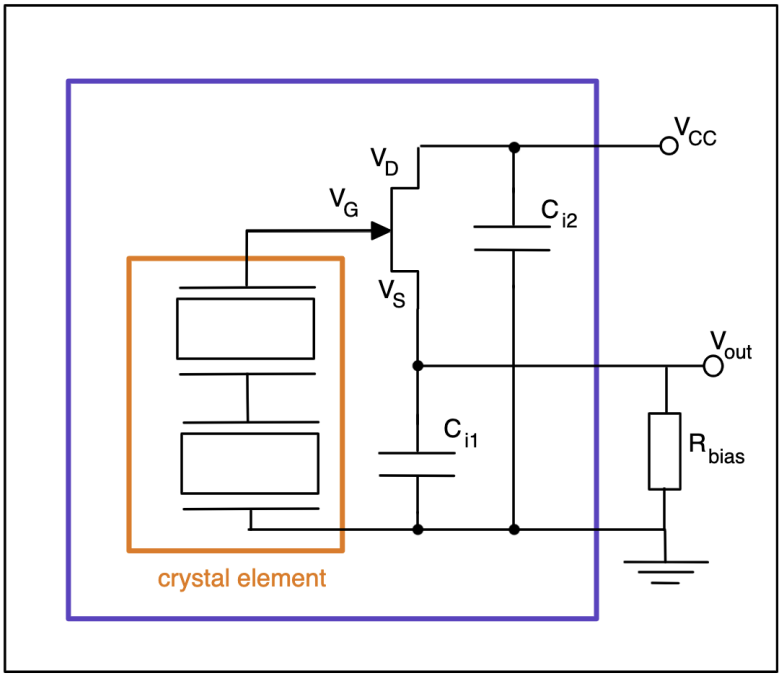

Figure 10: A circuit that combines the techniques mentioned so far: oppositely biased pyroelectric elements, a source follower, and smoothing capacitors. The purple box corresponds to what one finds on the sensor element PL-N823-01 [17] used for this thesis.

The main problem with this way of operating the PIR element is that one has a continuous current flow from V_{CC} through R_{bias} down to ground (provided that V_G is above or close to the threshold voltage of the transistor). It is desirable to reduce this current flow, as that would prolong the life of the sensor.

4 Algorithm for motion detection

Three algorithms for motion detection will be discussed. Firstly it will be shown that simple thresholding is a good starting point for a detection algorithm. Secondly moving thresholding will be introduced, which increases the robustness to environmental changes. Lastly, we will have a look at how batch averaging affects the algorithm. This is because some hardware implementations of the algorithm might be better implemented with batch averaging.

4.1 Simple thresholding

The orange line in figure 11 illustrates what a motion detection signal may look like.

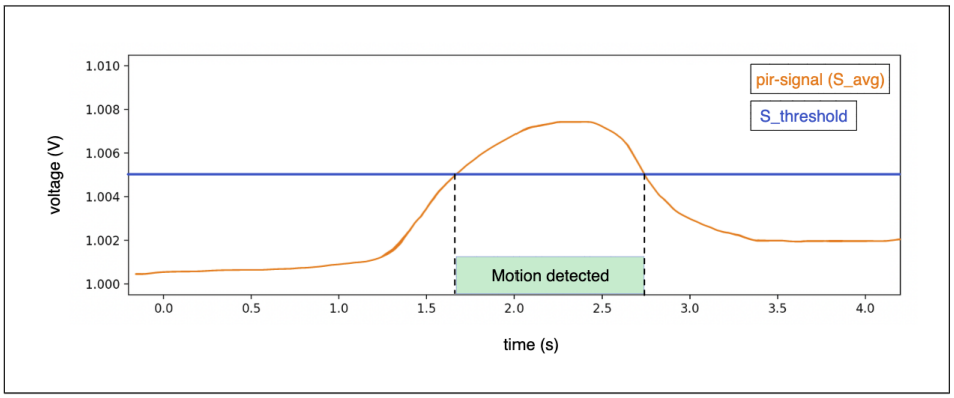

Figure 11: What a typical motion detection signal looks like.

As one can see from figure 11 the signal of a person moving in front of a PIR sensor increases, and as such a simple threshold is a good starting point for detection. If the pir-signal increases sufficiently (goes above our chosen threshold) it should be registered as a detection.

The green square and the blue line represent the place of detection and threshold respectively. The orange line is somewhat idealized and smoother than a sampled detection signal typically would be.

4.2 Moving thresholding

Simple thresholding is not particularly robust with regard to environmental changes, since it relies upon a hardcoded value for the threshold. If the normal values for the baseline of the signal were to drift from what one expects, due to for instance the average temperature of the room changing or factory variations between chips, the threshold might no longer be correct.

In order to solve this, one could use moving thresholding. Then the threshold is a function of the average measured values, and through that adapts relative to the baseline and the environment with no person present. Figure 12 explains the algorithm for detection with moving thresholding. Figure 13 shows an example of the intermediate and final signals from the detection algorithm. The color coding of the signals is the same for both figures.

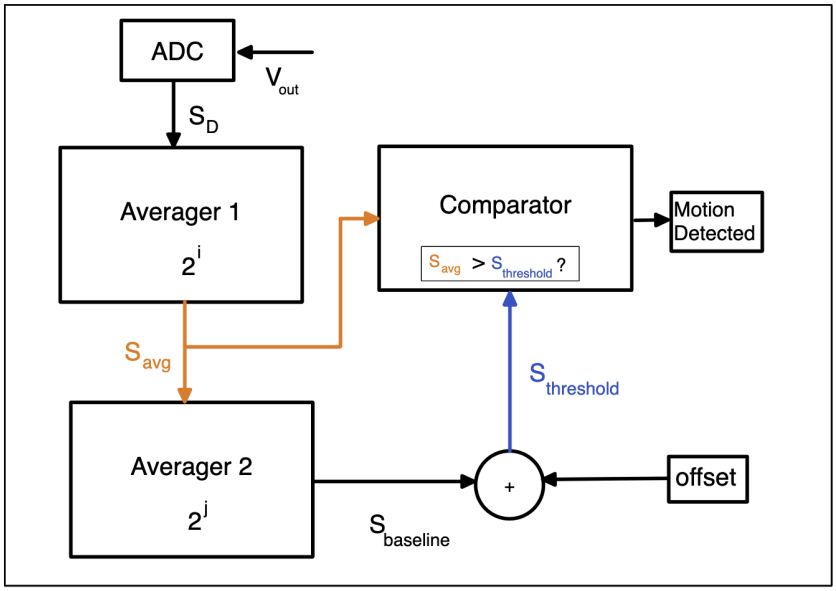

Figure 12: A detection algorithm with moving average. The measurements are averaged, and compared to a threshold. A detection is the same as the averaged signal being above this threshold. This threshold is dynamic, in order to compensate for drift in the system or the environment.

In figure 12 it is shown that the voltage we get out of the AFE, V_{out}, is sampled by an ADC, providing a digital signal S_D. The signal S_D that we get out of an ADC is first passed through an averager in order to reduce noise. The number of samples averaged in the averaged signal S_{avg} is 2^i. This signal is shown as the orange line in figure 13, and given in (4).

$$S_{avg}[n] = \frac{1}{2^i} \sum_{k=0}^{2^i} S_D[n-k] \tag{4}$$

The threshold to which S_{avg} is compared is not a hardcoded value, but rather we use an offset and a drifting baseline to compensate for changes in the environment. This drifting baseline $S_{baseline}$ is created by averaging S_{avg} by a factor 2^j, as given in (5)

$$S_{baseline} = \frac{1}{2^j} \sum_{k=0}^{2^j} S_{avg}[n-k] = \frac{1}{2^{i+j}} \sum_{k=0}^{2^{i+j}} S_D[n-k] \tag{5}$$

A static offset is added to this baseline, such that an increase in the signal is required for it to cross the threshold, as given in (6).

$$S_{threshold} = S_{baseline} + offset \tag{6}$$

The condition for detections being registered is expressed in (7), both in a compact form and expressed in terms of S_D.

$$S_{\text{avg}} > S_{\text{threshold}}$$
$$\frac{1}{2^i}\sum_{k=0}^{2^i} S_D[n-k] > \left(\frac{1}{2^{i+j}}\sum_{k=0}^{2^{i+j}} S_D[n-k]\right) + offset \tag{7}$$

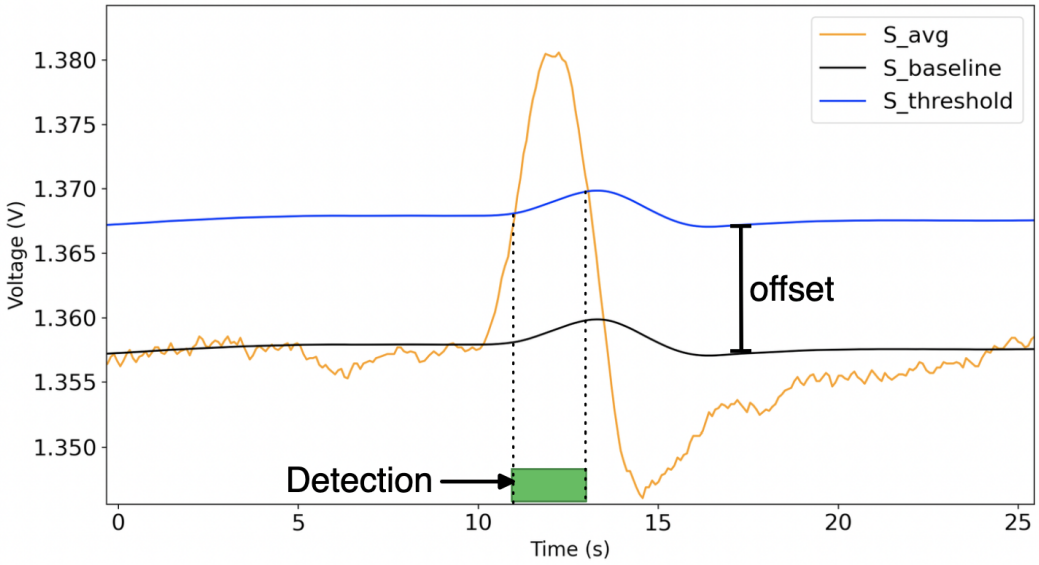

Figure 13: An example of the intermediate and final signals from the detection algorithm. Note how a detection (green box) occurs when S_{avg} (orange line), is above $S_{threshold}$ (blue line), as in the comparator of figure 12.

4.3 Batch averaging

In the particular low-energy hardware implementation of the moving thresholding algorithm used for section 11, batch averaging is used. We will therefore also take a look at how this affects the algorithm.

In batch averaging one sums the samples into an accumulator, and when 2^i (in the case of S_{avg}) samples have been collected, one divides the accumulated sum by 2^i. After this, the accumulator is zeroed out, and the process repeats. This means that all we are doing is still just averaging the signal, but we do so at more discrete time steps. Because of this, the only difference in the equations for batch averaging as compared to continuous averaging will be that the limits are less elegant. The equation for the batch-averaged signal $S_{avg,batch}$ is given in (8), and the limits are explained visually in figure 14.

We introduce the variables N, A, B, and C to be used solely in this section, to help us understand the limits of batch averaging. N, not to be confused with n, is the number of samples we average. In the case of $S_{avg,batch}$ we have $N = 2^i$. A and B are defined in figure 14 and represent times at which we update the signal $S_{avg,batch}$. If $n \in [B, C\rangle$, the samples to be averaged are $[A, B\rangle$. The reason the averaged signals are not in the range $[B, C\rangle$ for $n \in [B, C\rangle$ is that that would require us to know the value of the signal at times after n, and we cannot look into the future as this is a real-time system.

$$S_{avg,batch}[n] = \frac{1}{N}\sum_{k=A}^{B-1} S_D[k] = \frac{1}{N}\sum_{k=\left(\lfloor \frac{n}{N} \rfloor - 1\right)N}^{\lfloor \frac{n}{N} \rfloor N - 1} S_D[k] \tag{8}$$

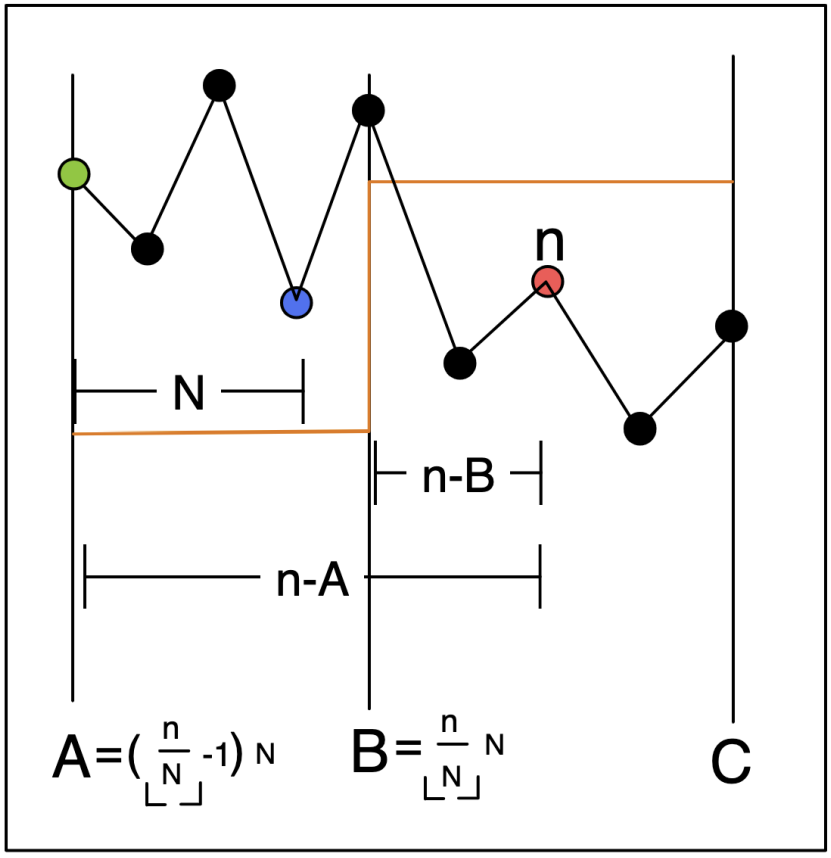

Figure 14: An illustration of the limits in batch averaging. A and B represent the times at which the averaged signal updates. N represents the number of samples to be averaged. If $n \in [B, C\rangle$, the samples to be averaged are $[A, B\rangle$. The green sample would be the first sample included in the average, and the blue sample would be the last. The orange line may represent $S_{avg,batch}$ and the black line S_D, with $N = 2^i$. Alternatively, the figure may equally well represent the orange line as $S_{baseline,avg}$ and the black line as S_{avg}, with $N = 2^j$. The figure uses N=4 for illustration, but in practice, N would be larger than this.

Flooring $\frac{n}{N}$ will give us the batch number n is in, rounded down. Multiplying the batch number by the number of samples in each batch will give us point B, which is the sample number of the first sample in the batch. This is shown in figure 14 and used in (8).

The total amount of samples averaged for creating the baseline will be $2^i \cdot 2^j = 2^{i+j}$. This means that for batch averaging the threshold will be updated every $t_s \cdot 2^{i+j}$ seconds, where t_s is the sampling rate.

The algorithm may be implemented in a low-energy IC. This would be relevant for a full low-energy motion detection system, as will be further discussed in section 11.

Section 10.6 discusses how different choices of i, j and $offset$ may impact the performance of the system.

5 Noise components background theory

Here relevant background theory for some different components of noise that we might have in the system will be presented. This analysis will be revisited in section 10.3, where we discuss the noise empirically.

There are many possible sources of noise in a system, and here we will look closer at quantization noise, thermal noise, noise from the pyroelectric element itself, noise from a power adapter, and miscellaneous sources of noise from control units. We will also discuss the effect thermal fluctuations in the environment may have on the measurement.

5.1 Noise bandwidth

The noise bandwidth Δf in a sampled data system has an upper bound given by the Nyquist frequency $\frac{f_s}{2}$. This is true even when aliasing occurs, as shown in [29]. This means that we have the relation

$$\Delta f \leq \frac{f_s}{2} \tag{9}$$

5.2 Quantization noise

As the analog signal is converted to a digital signal a quantization error is introduced. This is because we operate with discrete steps for the voltage level in the digital domain, rather than the continuous values we find in the analog domain.

The quantization noise power N_{quant} can be estimated as

$$N_{quant} = \frac{\Delta^2}{12} \tag{10}$$

where Δ is the quantization step. N_{quant} will also be equal to the mean square error between the digital and the analog signal.

5.3 Thermal noise of resistors

The thermal noise of a resistor is also called Johnson-Nyquist noise and its RMS (root mean square) value is given by

$$v_n = \sqrt{4k_{\mathrm{B}}TR\Delta f} \tag{11}$$

where k_{B} is Bolzmanns constant, T is the temperature in kelvin, R is resistance, and Δf is the noise bandwidth of the system. This was first shown in [16]. The noise power $N_{thermal}$ is independent of the resistance and is given by

$$N_{thermal} = \frac{v_n^2}{R} = 4k_{\mathrm{B}}T\Delta f \tag{12}$$

5.4 Noise out of pyroelectric element

Generally what is relevant to this is the noise of a resistor in parallel to a capacitor, because that is the construct you will get when using a small signal model of a transistor connected with a pyroelectric element. The resistance of the resistor is irrelevant to the noise in this configuration, and only the value of the capacitor matters. This is shown in [20]. We get the RMS voltage of this configuration as

$$v_{cap,parallel} = \frac{k_B T}{C} \tag{13}$$

Here k_B is Bolzmanns constant, and T is the temperature of the resistor.

5.5 Noise from a control unit and power adapter

A power adapter converts AC voltage to DC voltage which may result in a DC voltage that contains some noise. The AC input is typically rectified and passed through a filter. The filter reduces the ripple at the output, but might not completely remove it. Another issue with powering a system with a power adapter is that there may be noise from the power grid itself, which may be transferred into the system through the adapter. The connection to the adapter may also provide bigger ground loops that may introduce additional noise. Lastly, the adapter not only rectifies the AC voltage, but regulates the DC voltage, which introduces switching noise.

Powering a system with a power bank or a battery instead of a power adapter can alleviate this issue.

In section 7 a test rig for the system will be introduced. This test rig contains a control unit in the form of an RPi. The RPi is a digital system and may pollute any lines connected to it with switching noise.

Further discussion and measurements of both the noise from the RPi and power adapter can be found in section 10.3.

5.6 Thermal fluctuations in the environment

The basis of pyroelectric motion detection is that a change in temperature from a human entering the field of view of the sensor will cause a potential over the sensor element. However it is the case that other things may cause the temperature of the pyroelectric element to change, and there is no way to distinguish whether this temperature change is caused by a human or something else (provided that they cause the same temperature change).

We will call the signal caused by environmental temperature changes $S_{environ}$, and the temperature changes of a human entering the field of view of the sensor S_{human}.

$S_{environ}$ may be much bigger for an environment in which the system is placed next to an open window than when it is in the middle of an office space, as will be shown in section 10.3.3. Still, it will remain significantly smaller than S_{human} even when next to an open window, as will be shown in section 10.6.

$S_{environ}$ does not show up in the test rig that will be introduced in section 7. This is because, in that test rig, the sensor element is shielded from environmental temperature changes, in order to make the measurements more repeatable.

6 Proposal of alternate measurement circuit

Figure 15 shows the central idea of the new circuit proposed in this thesis. Figure 16 shows the measurement cycle for this circuit. Instead of having a biasing resistor R_{bias} through which a constant current is drawn, it is replaced by a capacitor C_m over which we measure the output. C_m will charge up until V_{out} is equal to V_G plus an offset.

The purpose of this change is to remove the power-hungry R_{bias}, but still replace it with something that can serve the same purpose in regards to providing a V_{out} that follows V_G.

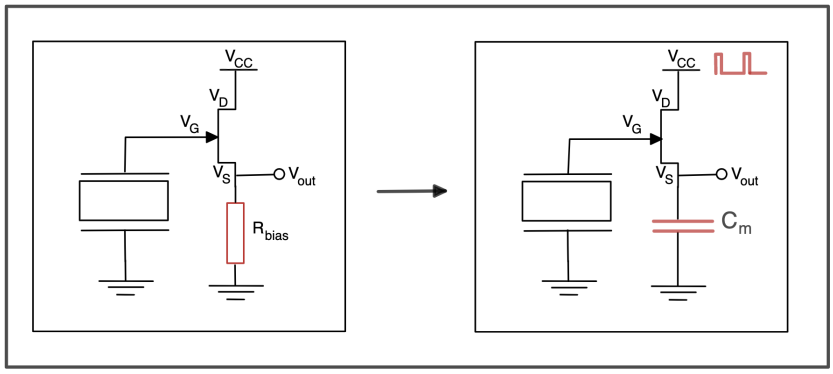

Figure 15: This summarises the central idea of the thesis. We replace the resistor R_{bias} with a capacitor C_m and duty-cycle V_{CC}.

Another very important change is that V_{CC} and V_{out} are treated differently in the new circuit. V_{CC} is duty cycled, as shown in figure 16. V_{out} is also pulled low during the time when the duty is low. This means that C_m is emptied between each cycle. During the high time t_{on} the capacitor C_m charges, and it is sampled at the end of t_{on}, before it is discharged down to ground. From the perspective of the ADC that measures V_{out}, the signal will still look pretty similar to figure 11, since in some regards the circuit can be thought of as an alternative to a source follower. It is the ADC that is responsible for pulling V_{out} to ground between measurements.

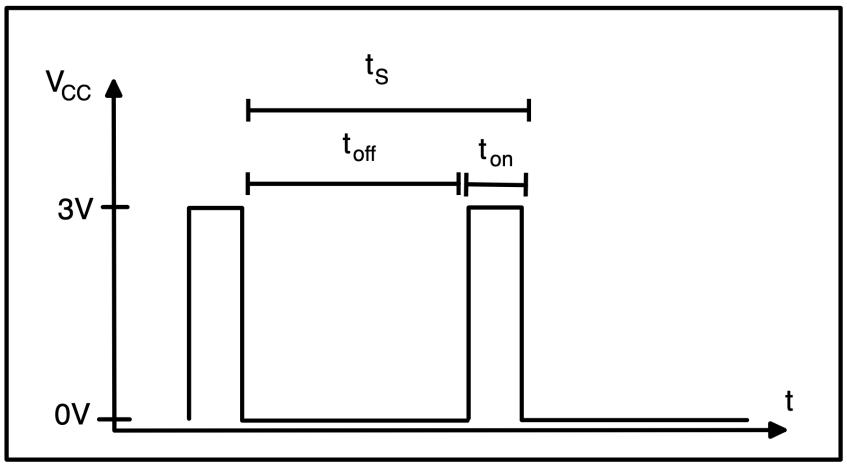

Figure 16: An illustration of duty cycling. V_{CC} is pulled high for a duration t_{on} and low for t_{off}. The sampling of V_{out} is done at the end of t_{on}. At the start of t_{on}, the capacitor between V_{out} and ground is completely discharged. This is because the ADC pulls V_{out} to ground during t_{off}. This will be further explained in section 10.1.

The alternate measurement circuit will still employ the moving thresholding algorithm described in section 4.2.

The power consumption of the circuit proposed here is given by

$$P = C_m \cdot V_{out}^2(n \cdot t_s) \cdot f_{sample} \tag{14}$$

Where f_{sample} is the frequency at which we sample V_{out}, which is the same as the frequency at which we duty cycle V_{CC}. We have the relation $f_{sample} = \frac{1}{t_s}$. $V_{out}(n \cdot t_s)$ is the voltage level of V_{out} at the time at which we sample it, that is, at the end of t_{on}.

From this, it is evident that the slower we sample the circuit the less power it consumes. The ratio between t_{on} and t_{off} is not as relevant. We still need to sample frequently enough to capture human motion, which has transients on the order of seconds.

It is also evident that the smaller we choose C_m, the less energy the circuit will consume. With a smaller C_m there will be less charge on the capacitor when it has reached V_{out}, which is ideal for low energy since that means less charge will flow through the circuit each measurement cycle.

An AFE using a normal source follower, as on the left of figure 15 will still work when duty-cycled. This will be shown in section 10.5.

There are two reasons that the resistor is changed to a capacitor. The main reason is that the ADC we will use for measuring V_{out} has a capacitance between its measurement port and ground, which means we would still have a capacitive path between V_{out} and ground when using the AFE on the left of figure 15. As a minor additional point, the topology on the left has been widely used in existing PIR sensors, and it is more interesting to explore new topologies.

7 Test rig

7.1 Test rig overview and dimensions

Figure 17 shows the dimensions and main idea behind the test rig. The idea is to control the radiation onto the sensor element in such a way that it is equivalent to a human passing the sensor. This makes the experiments more repeatable and precise. Understanding the measurement setup is important for understanding the measurements and the results of this thesis. The Peltier element is an element designed to keep a specific temperature that can be controlled depending on how much current passes through it. The Peltier element may either be exposed or hidden from the sensor element (Depending on the presence or absence of the removable sheet). This is equivalent to a person being outside or inside the sensor's field of view. The quantity to pay extra attention to in figure 17 is the distance between the top of the sensor element and the bottom of the Peltier element (4.7 cm) since this is relevant to how much heat is radiated onto the sensor element.

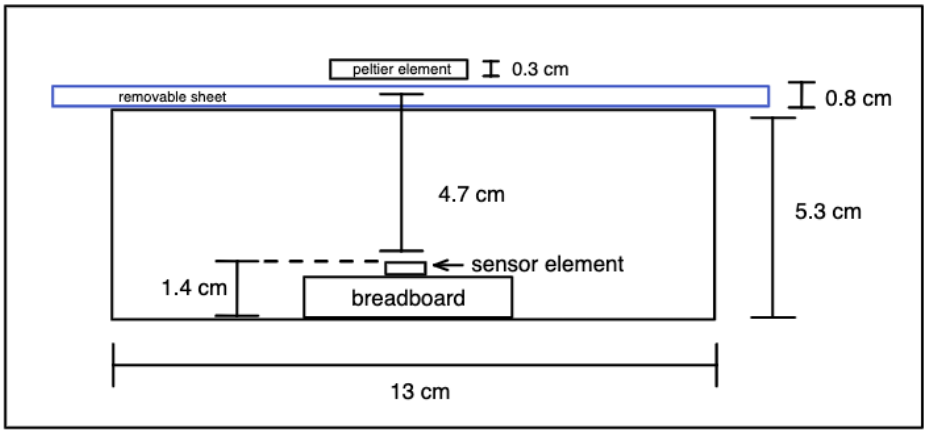

Figure 17: The dimensions of the test rig.

Controlling this system requires several components, as shown in figure 18.

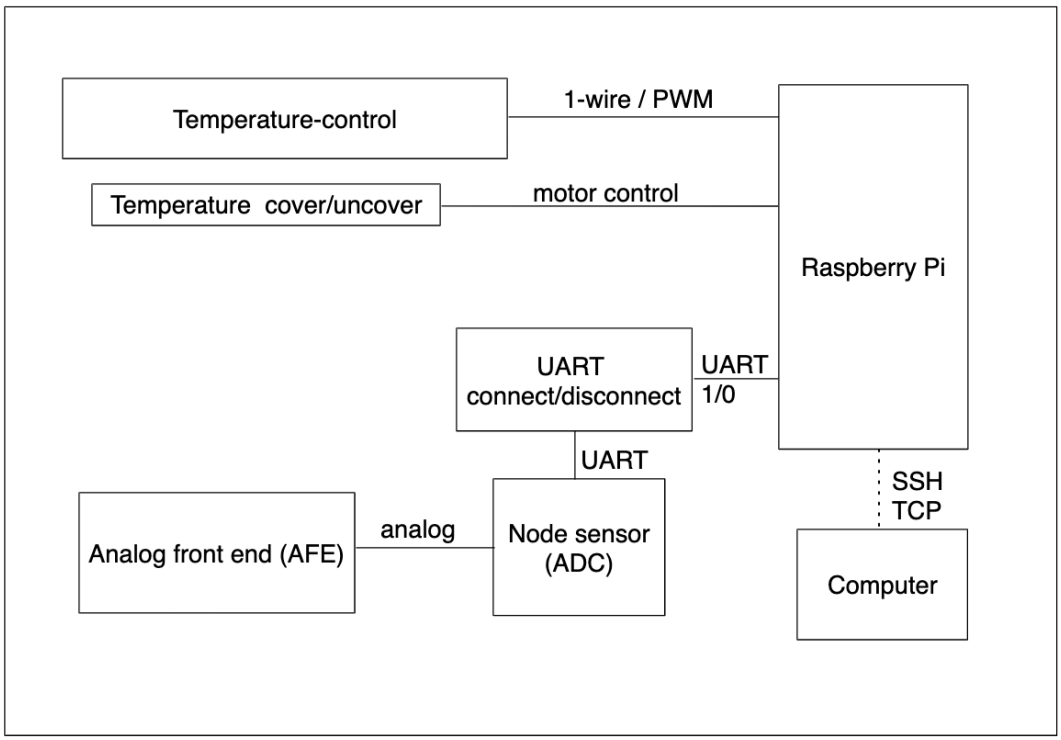

Figure 18: An overview of the test rig that was created for testing the pyroelectric measurement system.

The box labeled "Temperature control" in figure 18 is responsible for keeping the Peltier element at a stable temperature. It consists of a Peltier element, a temperature sensor, and some analog circuitry. It is further described in section 7.2.

The box labeled "Temperature cover/uncover" consists of a motor that controls the removable sheet in figure 17. It is further described in section 7.3.

The AFE consists of the pyroelectric element, and everything connected to it before the signal is converted to the digital domain. It is the same as the circuit proposed in section 6, and is shown in the right half of figure 15.

The node sensor is a measurement system that among other things contains the ADC. It is capable of sampling the analog signal and saving it to a buffer, which can then be read out by the RPi over UART. In section 11 we will see that the node sensor is a system on which one can build a complete IoT sensor node, but for now we will only consider it as an ADC with which the RPi measures the AFE.

The RPi communicates with the node sensor over UART. This connection can inject a significant amount of noise into the measurement, as discussed in section 5.5. We solve this problem by disconnecting the node sensor from the RPi, through a set of relays, when the UART-line is not in use. This is further discussed in section 7.4. [4] The measurement of noise injected by the RPi will also be discussed in 10.3.

Finding the parameters for ideal stimuli is discussed further in section 7.5.

[4] A custom program for interfacing the RPi and the node sensor through UART was written for this project. This includes several functions for the setup and control of the node sensor. This will not be discussed in any detail, as it contains information confidential to DT, as well as the fact that knowledge of this is not necessary for understanding the measurements.

The RPi, in addition to saving the measurements to a file, streams the data to a computer that shows a live plot. [5] Processing and analysis of the measurements are also done on the computer.

An image of the full test rig is shown in figure 19.

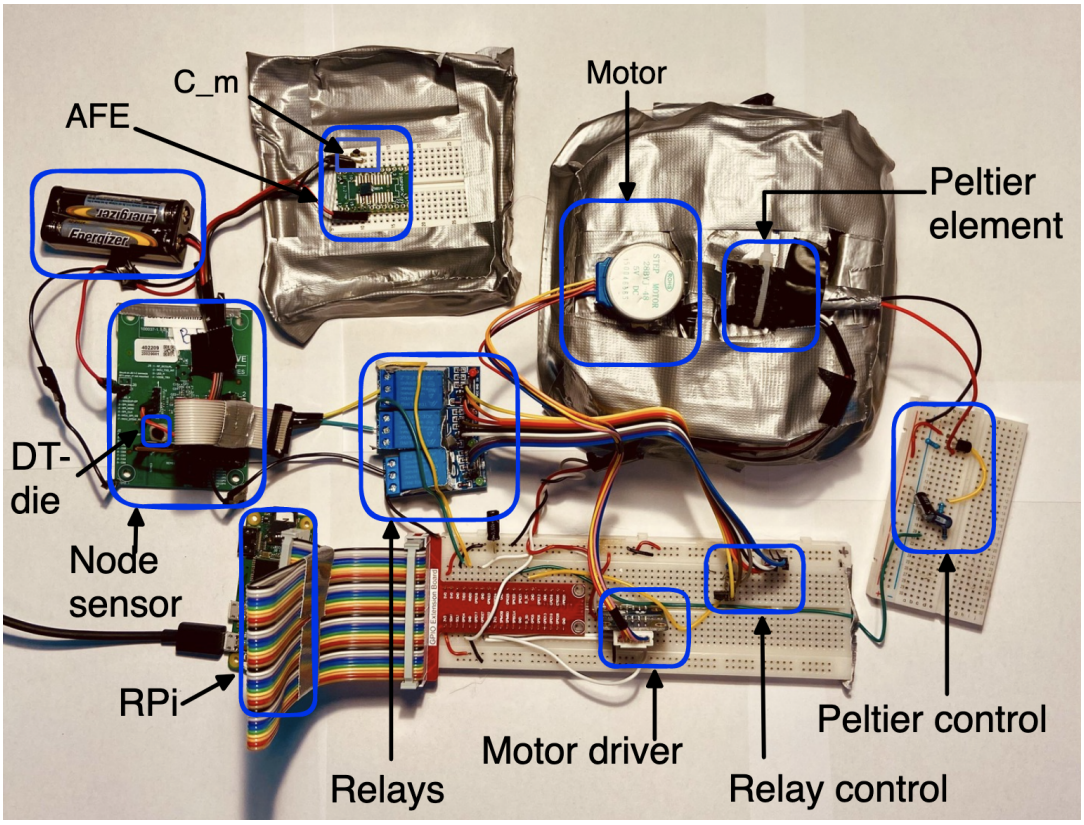

Figure 19: An image of the test rig used. The box on which the motor sits is covered in aluminum foil taped down, to create an isolation against IR radiation. The Peltier cover/uncover system is on the inside of this box. The temperature sensor is connected to the other side of the Peltier element. Normally the box on which the motor sits would be placed on top of the AFE.

7.2 Peltier temperature regulation

The Peltier element needs to keep a stable temperature, which requires regulating the current through it. This current is also more than what an RPi can source from any of its GPIO ports.

Figure 20 shows the circuit for controlling the current through the Peltier element with a GPIO port on the RPi.

The RPi does not provide an analog signal out from its GPIO ports. However, such an analog signal may be obtained by sending a PWM (Pulse Width Modulated) signal from the GPIO port through a low pass filter. The PWM is a square signal, and the ratio of the time it is high to the total signal period will determine the voltage we get out of the low-pass filter.

[5] This is done by piping the tail of the measurement file into Netcat which then sends the measurements over TCP, and on the computer end piping from Netcat into a Python program that plots using Bokeh.

The filter is a second-order filter.

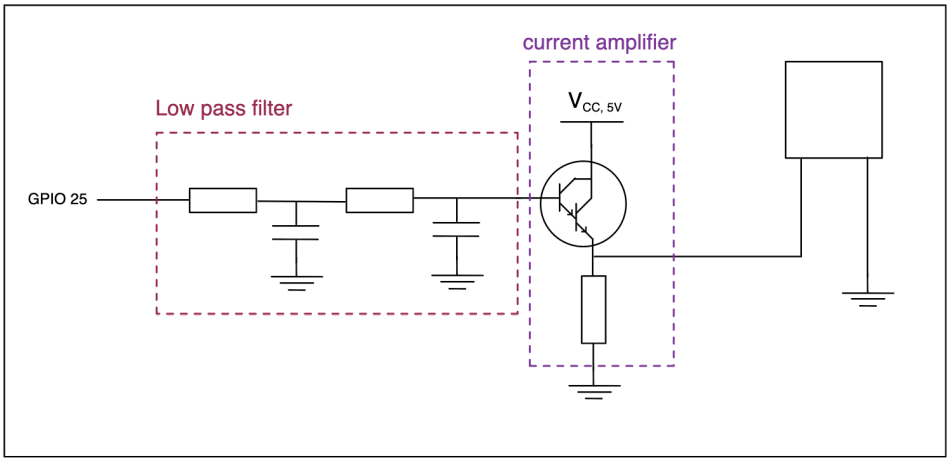

Figure 20: The circuit for Peltier element temperature control.

Drawing too much current from a GPIO port causes the RPi to crash. However, the 5V port is connected directly to the adapter that powers the RPi, which means it can source up to about 2A (depending on the adapter). This is why the low pass filter is followed by a current amplifier in figure 20. The current amplifier is a common collector amplifier, also called a voltage buffer. The transistor used is BC517 [3], which is designed for handling higher currents than most BJT transistors. It is constructed as a Darlington pair, which essentially results in better current amplification.

The Peltier element is APH-031-10-13-S [1]. The temperature sensor is DS18B20, which is a digital temperature sensor that uses the 1-wire interface. [9]

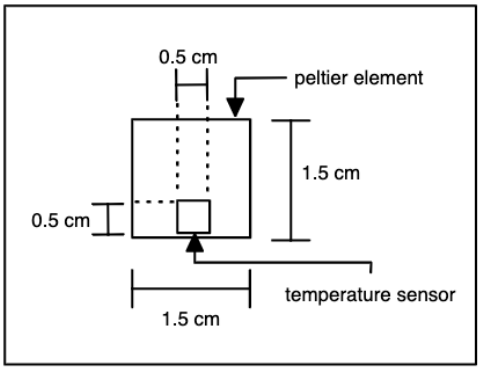

Figure 21: The dimensions of the Peltier element. The hot side of the element is connected to the temperature sensor used when regulating it. It is this side that faces downwards in figure 23. The other side has a heat sink connected to it, as can be seen in figure 19.

Now that we can control the current through the Peltier element all we need to do is to choose a value for it based on the temperature that we wish for it to have. To achieve this we first measure what temperature it is currently at (with a temperature sensor mounted directly on the element, as illustrated in figure 21). Then this temperature is fed back as an increase or decrease of the PWM signal. The feedback loop that regulates this is a

simple PID (Proportional-Integral-Derivative) controller, implemented in software on the RPi. [6]

7.3 Temperature on/off

The Peltier element can not in itself produce a temperature gradient sufficient to simulate a person entering the field of view of the sensor. Because of this, we use a method involving covering and uncovering the Peltier element, from the perspective of the sensor element.[7] A top view of this is shown in figure 22, and a side view of this is whoen in figure 23. The motor that is used is 28BYJ-48 [23] with a ULN2003 driver [28]. The motor is not continuously rotating, but rather turns back and forth when prompted, to uncover the Peltier element for two seconds.

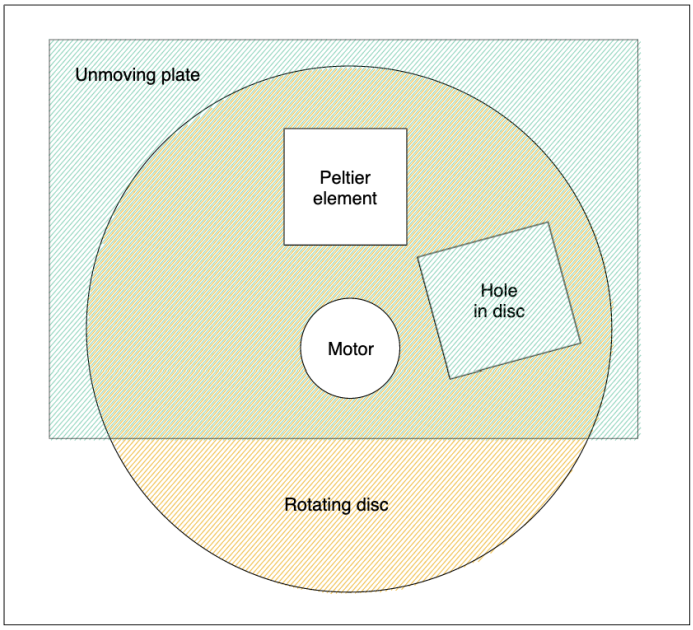

Figure 22: Top view

[6] The values for the PID regulators were $K_p = 1$, $K_i = 0.1$, and $K_d = 0.05$, with an update rate of 1 second. K_p, K_i and K_d are respectively the proportional, integral, and derivative gain. These values were found empirically to provide a stable temperature.

[7] As an analogy we may think of it as the Peltier element playing "peek-a-boo" with the sensor element, and the rotating disc being the hands. The unmoving disc would be the shoulder/neck that keeps both the hand and face in place.

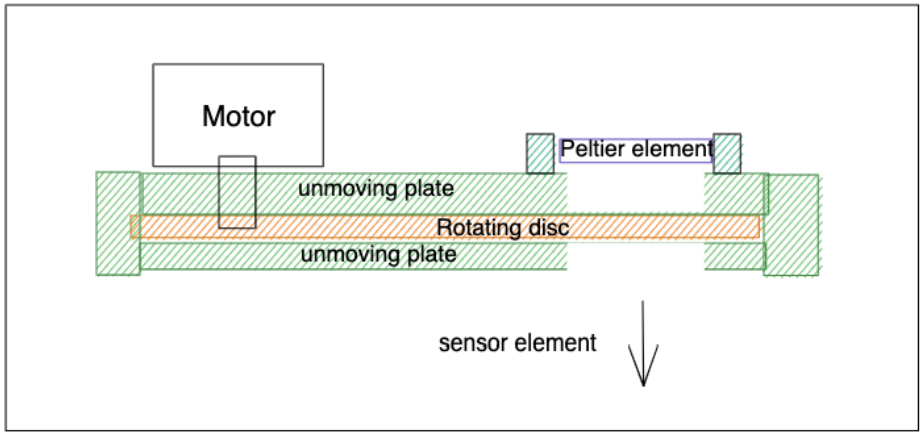

Figure 23: Side view

7.4 UART connection noise reduction

The node sensor is sensitive to noise from UART, as discussed in section 5.5, and as will be demonstrated further in section 10.3.

Initially, the RPi communicated with the node sensor for every sample taken, streaming the samples directly over UART. This means that the UART ports are toggled far more than strictly necessary, which may inject noise into the node sensor.

To reduce this we instead do a multisample. During a multisampling, the samples are saved to a buffer that is stored locally on the node sensor. All that the RPi does is initiate the multisampling, and then read out the buffer once the sampling is finished. This significantly reduces the toggling.

However, the RPi still injects noise into the measurements. To avoid this one can physically disconnect the wires between the node sensor and the RPi during the multisampling. This can be done with relays, as shown in figure 24. The relays that are used are of type JFQ-T73 [13].

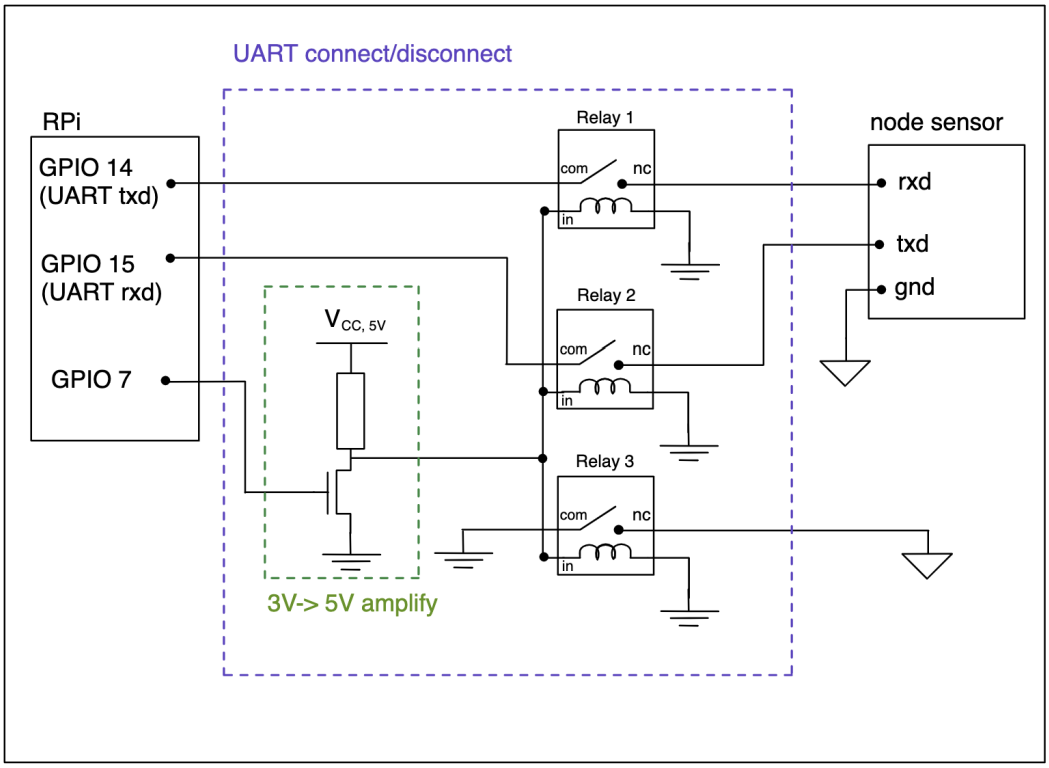

Figure 24: This illustrates how relays are used to disconnect the UART lines when they are not in use.

GPIO 7 on the RPi is used to control all the relays at the same time. It is first passed through an amplifier because the relays require a 5V input to toggle. The amplifier is inverting.

7.5 Finding equivalent signal

If the signal S_D is the same for the measurement in the test rig as it is for a person passing below the sensor, this must mean that they provide the same heat flux onto the element. In that case the signal measured in the test rig will be representative of the signal from a person passing the element. This equivalent signal is achieved when the Peltier element is 33°C. This was tested by making a measurement with a person walking past a sensor element mounted in the ceiling, and then comparing it to what scenario in the test rig provides the same signal. The room temperature was 22°C the height of the person was 180cm and the height up to the ceiling is 2.5m. This is illustrated in figure 25.

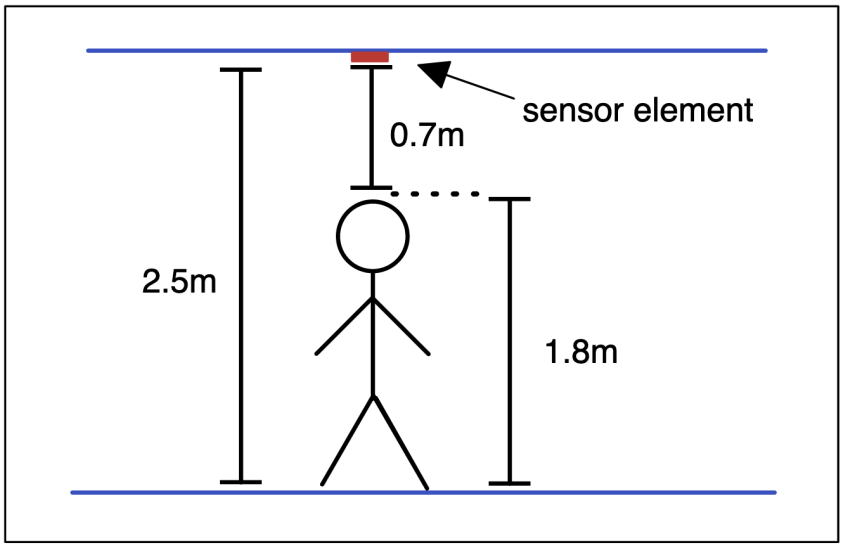

Figure 25: A person passing a ceiling-mounted sensor. These are the particular dimensions of the test used as a reference to calibrate the test rig.

Figure 26 shows a comparison between the signal of a human walking past the sensor.

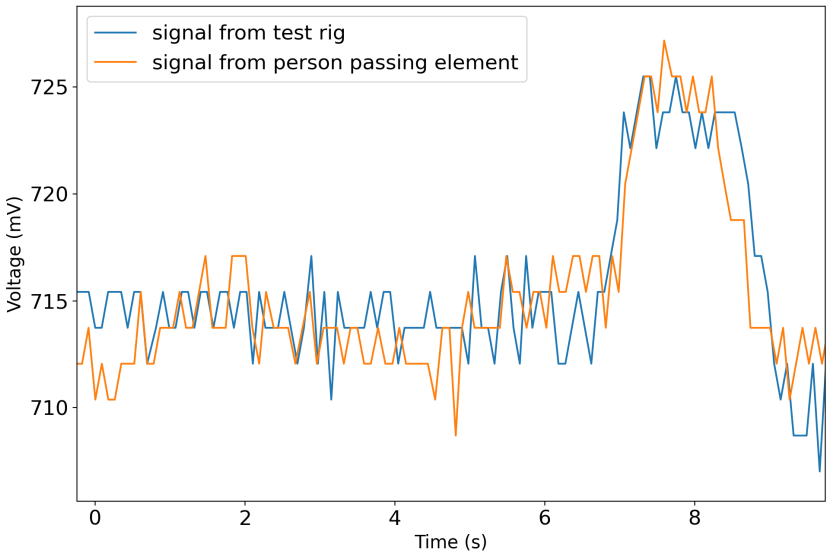

Figure 26: A comparison between the signal from a person passing the sensor, and the pir-jig with the Peltier element at 33°C.

Humans come in all sorts of heights and sizes and might be wearing headwear or have slightly different body temperatures. Rooms may be different temperatures and heights. Because of this, there is no single signal that will fit exactly all situations where the sensor should detect human presence. The signal in this section is chosen because it seems representative of relevant use cases, but this caveat should be kept in mind.

The thermal flux experienced by the sensor element as a person passes below it is discussed in appendix D.

8 Modification of sensor element

The sensor PL-N823-01 [17] is used in this thesis, as it provided promising initial measurements.

The sensor element must be modified as shown in figure 27 to be of use for the low-energy circuitry proposed in this thesis. The subject of this section is the practical concerns regarding this modification. [8]

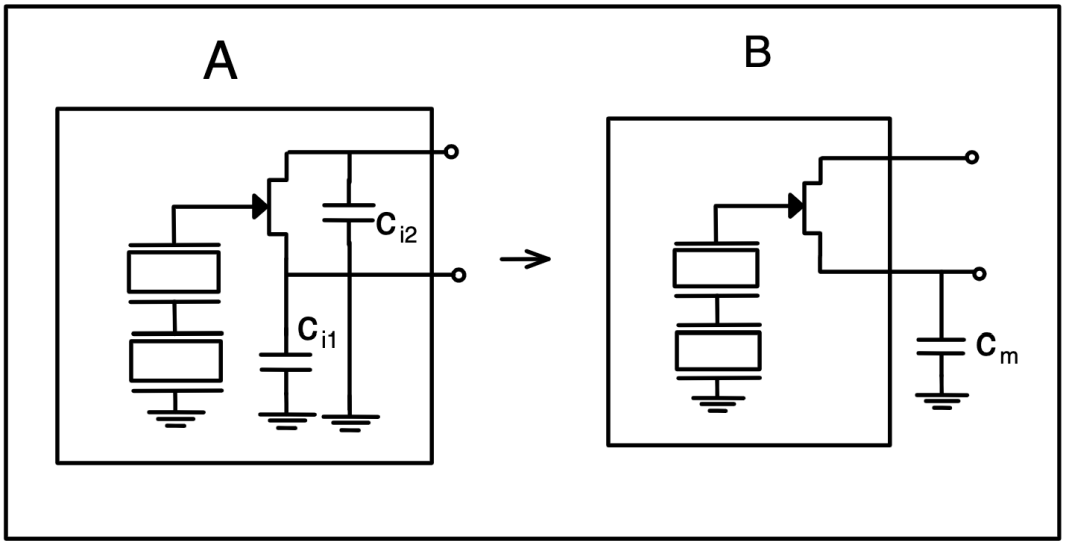

Figure 27: The disassembly of the sensor. Circuit A is what the unmodified PL-N823-01 chip looks like[17]. In circuit B the capacitors inside PL-N823-01 have been removed and we added a capacitor C_m instead.

If circuit A is duty cycled it will burn a lot of unnecessary power because of the two 2nF capacitors that are charged and discharged for each measurement. That is the reason for removing these capacitors from the sensor. We still need a capacitor to be charged and measured, so we add capacitor C_m, resulting in circuit B in figure 27.

In order to access these components it is possible to use a diagonal plier to apply force about midway up on the side of the sensor, as shown in figure 28. If done correctly the "lid" (top part) of the sensor will pop off cleanly (and remain intact) and one is left with access to the components as shown in figure 29.[9] The schematic in figure 27 A corresponds to the physical circuit shown in figure 29.

[8] Note that the sole purpose of the sensor disassembly is to obtain a component to work with, that is not readily available off the shelf, not to reverse engineer the IP of Kemet (the manufacturer of the sensor).

[9] This may take a couple of attempts to master, and it is recommended to have some extra sensor elements at hand.

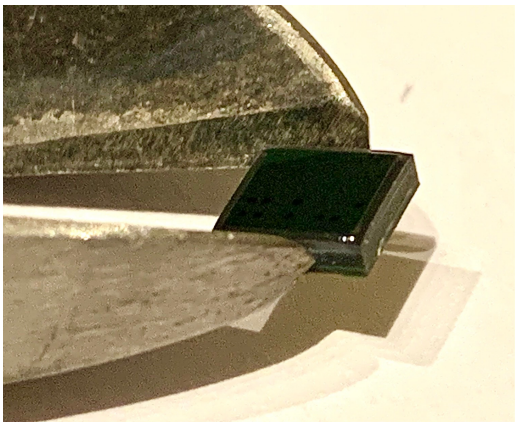

Figure 28: Where to apply pressure to the sensor in order to disassemble it. Note the colors of the layers of the sensor. The metallic top part is the "lid", and the green bottom part is a PCB board. The middle grey part surrounds a hollow space in which one finds the surface-mounted components depicted in figure 29. The ideal place to apply pressure is right beneath the lid.

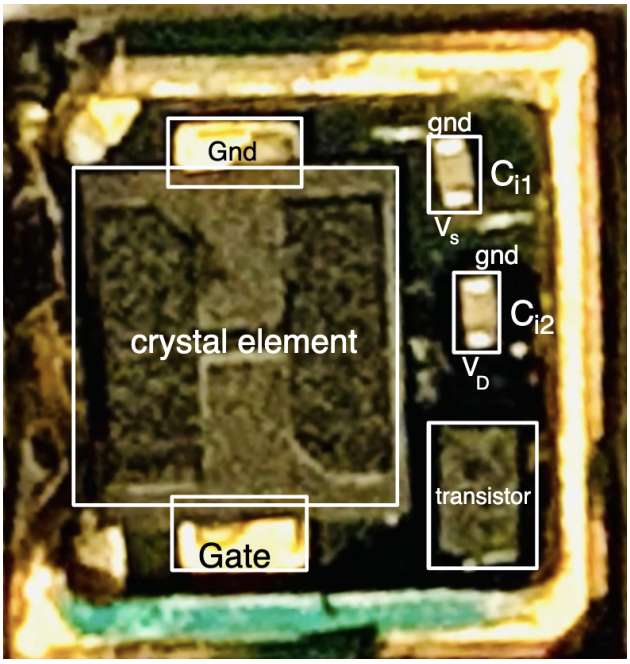

Figure 29: Disassembled sensor. The "lid" of the sensor has been removed, and we can see discrete surface-mounted components inside the sensor element.

Testing shows that the behavior of the sensor is practically unchanged if one removes the lid and then places it back on top, so no important thermal properties of the sensor are affected by this. [10]

With the lid removed one can use a soldering iron to remove the internal capacitors (C_{i1}, C_{i2}). Care should be taken when doing this, and it is important to avoid touching the pyroelectric element. The element breaks easily if touched, as it is very brittle, and it

[10]The lid modulates the signal in such a way that a Fresnel lens is optional. For the measurements in the thesis, no lens was used. For the prototype presented in section 11 the fresnel lens of type "natural lens" [17] was used.

is based on PZT which contains lead and is toxic. For more information regarding safety precautions when handling PZT, refer to [15].

8.1 Measuring the transistor

What transistor PL-N823-01 used is not in the datasheet[17].[11] Despite this, it is possible to find a transistor that has equivalent IV curves to it, which is all that is needed for a simulation model. That transistor is TF412S from ON Semiconductor [26].

One can remove the transistor from the sensor element and measure the IV curves for it. The result of this measurement is shown in figure 30A. A parametric search based on these IV curves yields only one transistor. The IV-curve of TF412S is shown in figure 30B. Note the almost exact correspondence between the curves. The axes of the two plots are not the same height, and the legends are slightly different, but this is only a visual difference, the IV curves are practically identical.

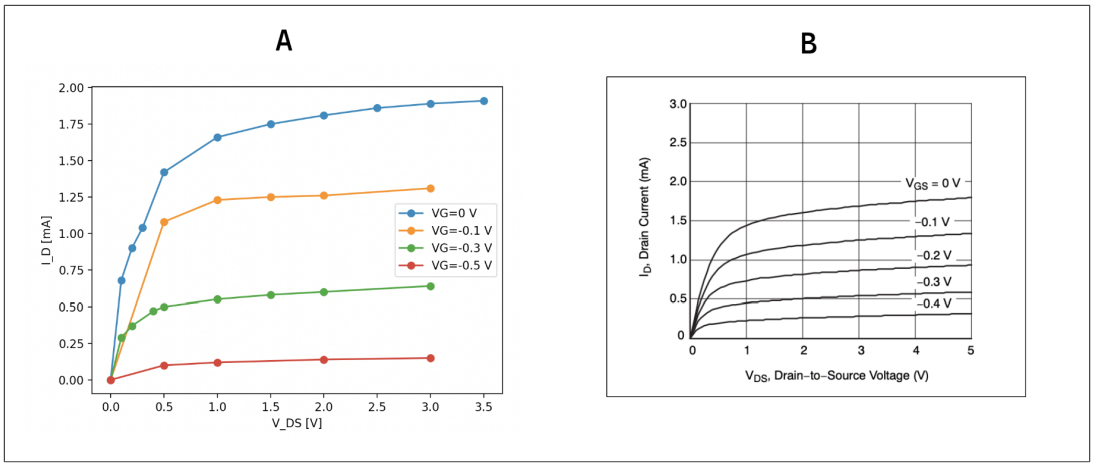

Figure 30: The measured IV-curve of the transistor in PL-N823-01 is shown on the left. The IV-curve of TF412S (as taken from its datasheet [26]) is shown on the right. Note the striking resemblance between the two.

The transistor has a Spice model given in appendix B.1, as will be further explored in section 9 that discusses simulating the system.

9 Spice simulation circuitry

9.1 Top level cicuitry

Figure 31 shows the top-level simulation circuitry for our system. It provides an output "V_out", which ideally should be similar to what we measure empirically. The left part of the circuitry, marked "Sensor element" should be similar to the actual sensor element. It

[11] No information regarding the internal transistor of PL-N823-01 is publicly available. When this was requested by mail, Kemet (the manufacturer of the sensor) were unwilling to provide this, as they said it was "company confidential".

contains a model of the pyroelectric element, which gives an output "V_p". The subcircuit for it is described in section 9.3.

It also contains a model of the transistor used in the sensor element. The model used is for transistor TF412S, as discussed in section 8.1. The Spice listing for this transistor may be found in appendix B.1. The full Spice listing for the circuitry described in this section may be found in appendix B.2.

The right half of the circuitry, labeled "DT-die", is responsible for making sure that the potential at Drain and Source is similar to what it is in reality. It is not a complete representation of the DT-die ADC, as that ADC is a very complex circuit. However, as seen from the perspective of Drain and Source pins, it should still be similar. The subcircuit for this is described in section 9.2.

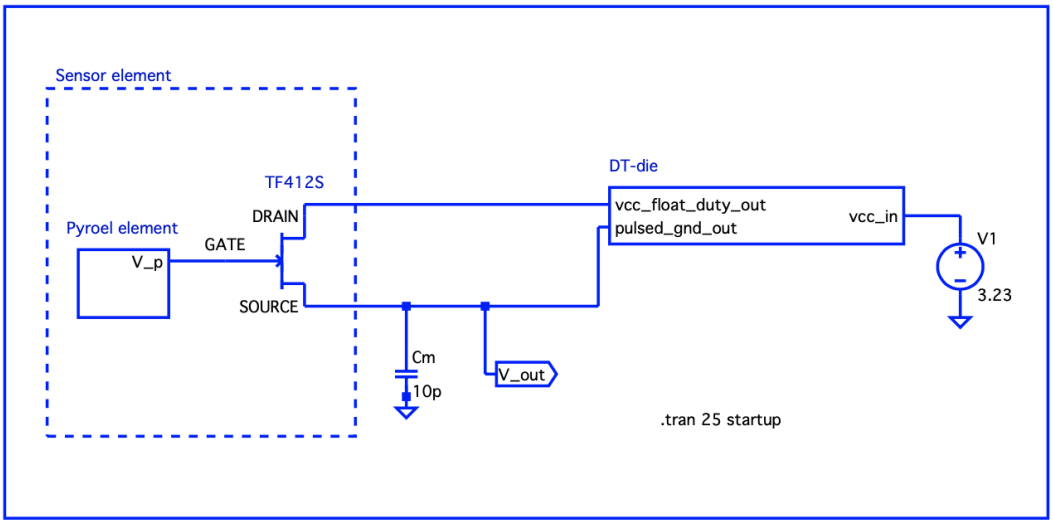

Figure 31: The top-level circuitry of the simulation.

9.2 Duty cycling circuitry

The measurement apparatus (DT-die) pulses ground and VCC as described in section 6, and is shown in figure 32.

The cycling circuitry shown in figure 32 receives a pulse_control_in, which is a square wave, and provides a similar wave out on vcc_float_duty_out and pulsed_gnd_out. The difference between the output and the input is that the pins float when not at their respective level. That means that vcc_float_duty_out alternates between VCC (as provided by vcc_in) and floating. The signal pulsed_gnd_out alternates between ground and floating. This is the same as what the ADC in the DT-die does.

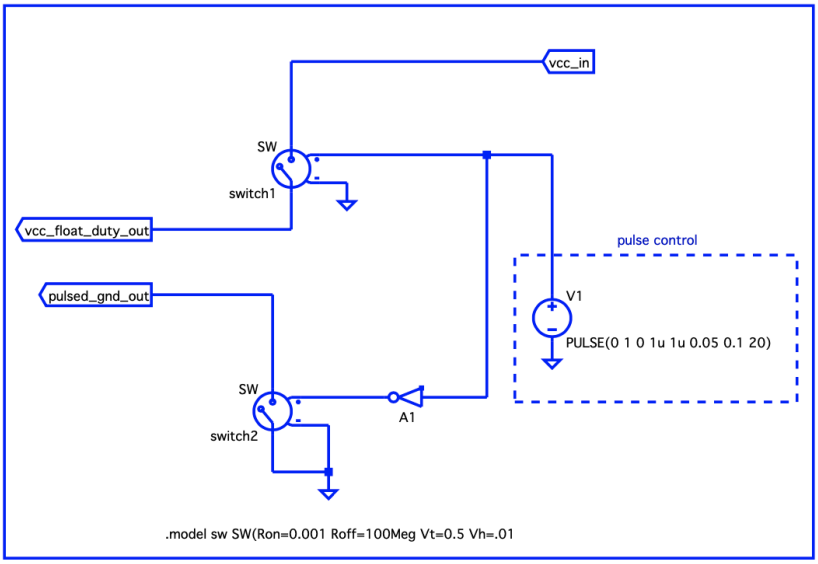

Figure 32: The circuitry for the cycling submodule. It has an output vcc_float_duty_out that alternates between being connected to V_{cc} and floating. It has another output that alternates between being pulled to ground and floating. It has an input that should be a square wave, which controls the period of cycling.

Unfortunately, the DT-die has an internal capacitance $C_{ADC} = 20\text{pF}$. It also has a biasing current $I_{bias,ADC} = 1.0715\mu\text{A}$. It would be preferable if these were both zero, but that is not the case with this particular ADC. The complete circuitry we use for simulating the DT-die is shown in figure 33.

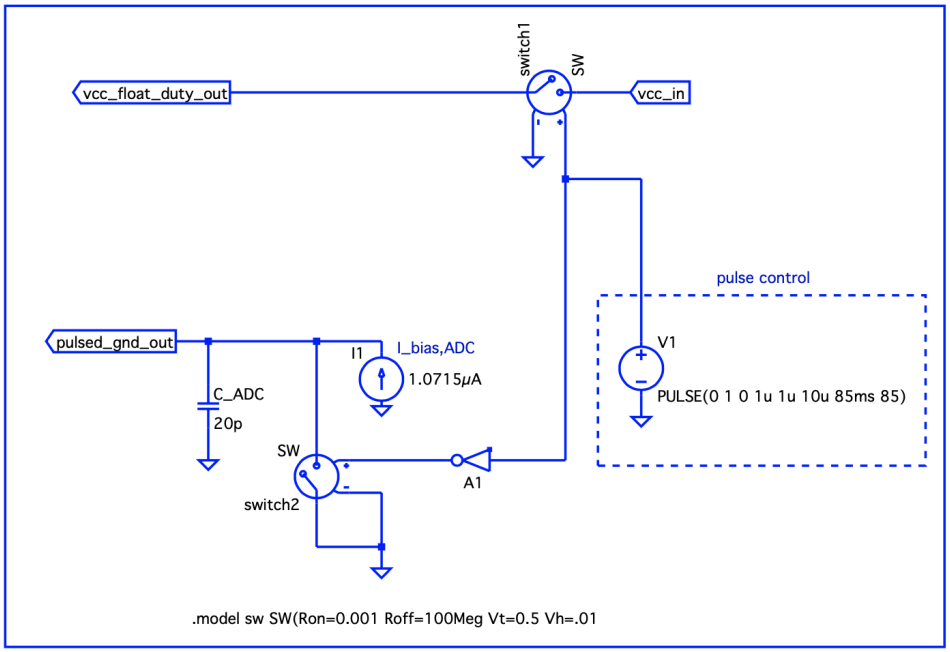

Figure 33: The ADC has an internal capacitance C_m and a biasing current $I_{bias,ADC}$. These have been added here. Other than that, the circuitry is identical to that shown in figure 32.

9.3 Pyroelectric element Spice model

The Spice model for the pyroelectric element is shown in figure 34. This corresponds to figure 3 from section 2.2 in which the theoretical equivalent pyroelectric model was discussed.

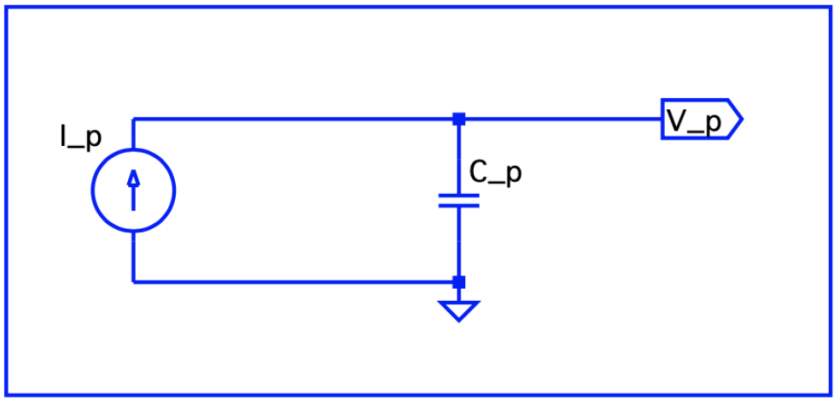

Figure 34: This is the submodule that is responsible for giving out a signal equivalent to the output of a pyroelectric element. The picture is a screenshot of the model in LTspice.

10 Signal quality of the system

In this section, we will pull a lot of threads from previous sections together, and show in practice what sort of signal quality we can achieve.

First, the insights gained from the simulation are presented. This includes an explanation of the relation between $V_{out}(t)$, $V_{out}(n \cdot t_s)$ and S_D, as well as a discussion regarding the mechanisms that cause the DC level of our signal. Then, some insights from particular measurements are presented. This includes a set of measurements in which we identify which components of our system cause noise, and the degree of noise they cause. This noise analysis will reveal that practically all the noise we observe is caused by the digital circuitry, rather than the AFE. Once we have analyzed the noise we will analyze the signal. This discussion will find that the signal has the same amplitude regardless of what value one chooses for C_m. Once this is in place, how well the system works for different parameters of the detection algorithm will be discussed in section 10.6.

10.1 Simulation sampling

The blue line in figure 35 shows a simulation of V_{out}. Note that some values in the simulation have been exaggerated to make the figure more readable, so this particular figure does not have representative quantities. More representative simulations will be presented later.

The orange line is a sampled version of the given by the relation $V_{out}(n \cdot t_s)$, where t_s is the sampling period, and n is a natural number. [12] This is as explained in section 6, and illustrated in figure 16.

[12] This sampling is done by importing the simulation output from V_{out} into python, and using a resampling function.

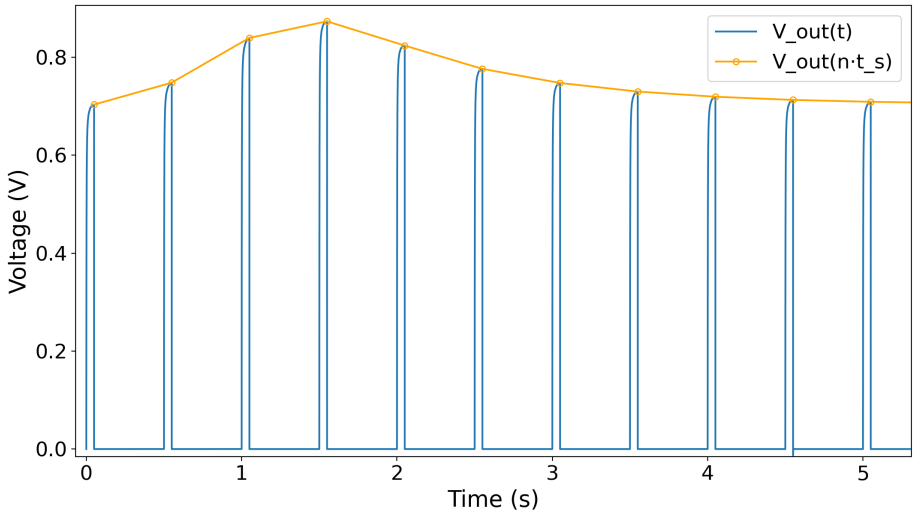

Figure 35: An illustration of sampling of signal V_{out}. The values of the voltages, as well as the sampling times, are vastly exaggerated in the simulation pictured here.

Figure 36 illustrates the point at which the ADC samples its input, which is in correspondence with figure 16, but here the transient charge-up curve is shown as well. Figure 36 is a zoomed-in view of one of the charge-up curves in figure 35.

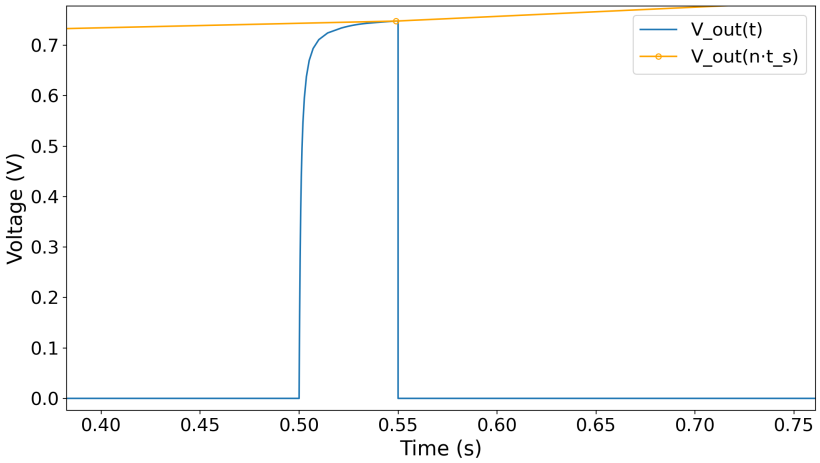

Figure 36: A zoomed-in view of a single transient. It is sampled at time t_s when it has reached its maximum.

Figure 37 is the same plot as figure 35, except that $V_{out}(t)$ is not shown. This signal almost gives us S_D, the signal we would get out of the ADC, introduced in figure 12. We just need to add the quantization error Δ, and we obtain the relation

$$S_D = V_{out}(n \cdot t_s) + \Delta \tag{15}$$

In section 10.3 This quantization error, combined with digital switching noise, will be

shown to be what constitutes the biggest source of error in our measurement.

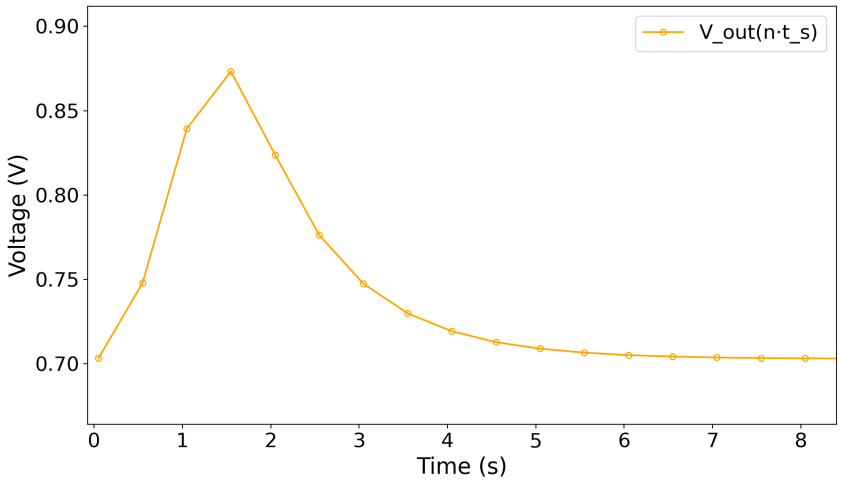

Figure 37: This figure is a plot of $V_{out}(n \cdot t_s)$, still for some very exaggerated values of the simulation. It is the same as figure 35, except that the plot of V_{out} is not shown. This signal is also the same as S_D, except that S_D also has a quantization error.

Figure 38 shows a more realistic simulation, overlaying a measurement. It is more realistic in that $t_s = 0.1$s and $t_{on} = 10\mu$s are equal to what they were for the measurement, and that $C_p = 43$pF (which is realistic in regards to (1) and the approximate size of the element). For the measurement and simulation $C_m = 5.6$pF.

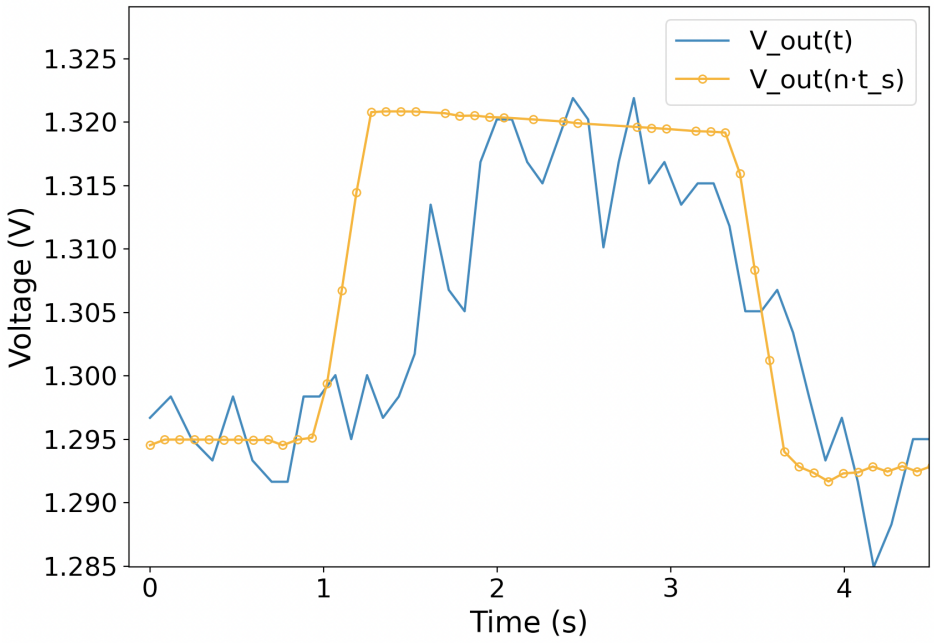

Figure 38: An overlay between the simulation and measured values.

Appendix E discusses the simulation in further detail. This includes a discussion regarding how I_p is chosen, some caveats regarding the simulation, as well as some more plots of the

simulation and measured values.

10.2 DC levels

For successful detection with the algorithm described in 4.2 what we are interested in are the small signal variations of our digital signal. However, let us for a moment discuss the DC level of the digital signal, as this might provide us with some important insights, even though it seems (and is) irrelevant to how well detections are made.

Figure 39 shows that the measured S_D may reach a voltage of around 1.48V even with no motion present. If the gate of the transistor was controlled by a DC voltage source, and we ignore $I_{bias,ADC}$, the gate voltage would have to be around 0.8V. [13] This is significantly larger than 0V, which is what one could expect to get out of the pyroelectric element when there is no motion present.

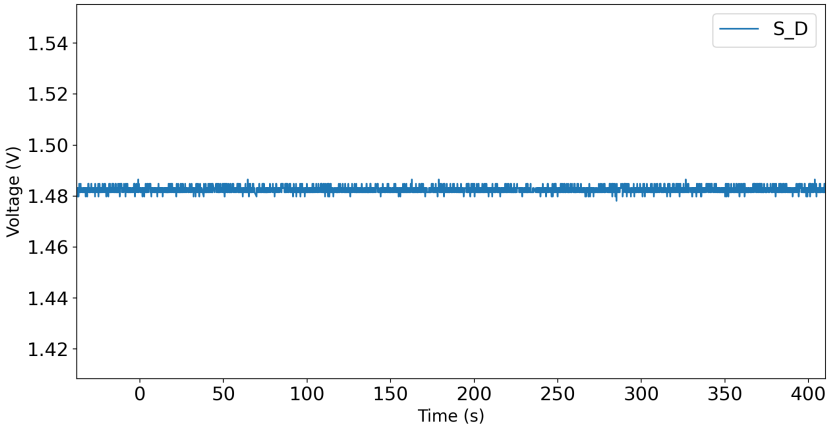

Figure 39: This is a measurement showing S_D with no motion in front of the sensor element. In order to reach this voltage the gate voltage would have to be much higher than what one might expect. In this section, we look further into why it reaches this voltage.

A first candidate for explaining this would be $I_{bias,ADC}$, considering as we just ignored it so far. $I_{bias,ADC}$ causes V_{out} to increase regardless of V_G. However, figure 40 shows that this is not a sufficient explanation.

It illustrates that the bias current adds about 0.25V to the DC offset, which is not enough to account for the offset shown in figure 39.

Normally V_{cc} would go high at the same time as $I_{bias,ADC}$, but for illustration purposes, they are clocked with different clocks in figure 40, so that V_{cc} goes high a bit earlier. Figure 40 also gives us insight into the charge-up speeds before the transistor saturates, which is much shorter than t_{on}. The point at which it saturates is dependent on V_p, applied to the gate of the transistor.

[13] This voltage of 0.8V was found by controlling V_p with a voltage source and adjusting it until V_{out} reaches 1.48V, in simulation (without having $I_{bias,ADC}$ connected in the simulation circuitry).

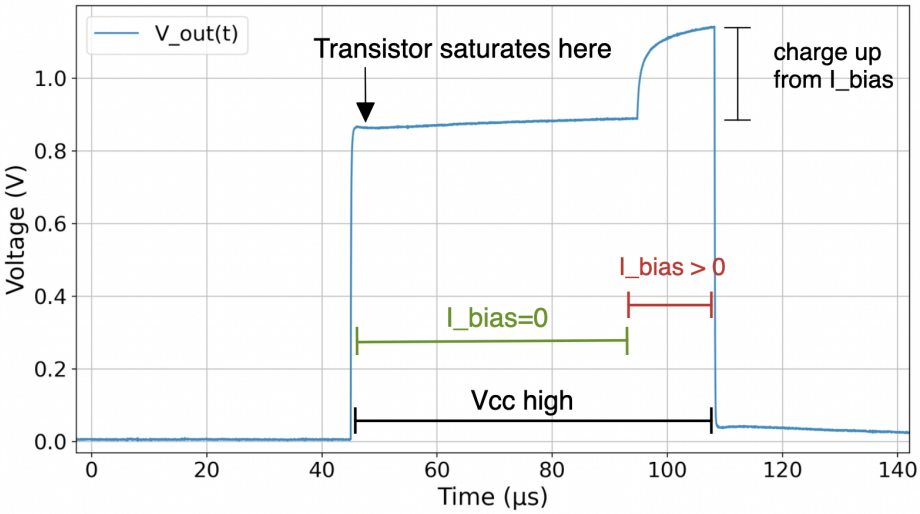

Figure 40: A measurement of V_{out} with an offset to the clock controllng V_{cc} so that it goes high before $I_{bias,ADC}$. The measurement is done with an oscilloscope. The oscilloscope causes a slight decrease in the signal since it has an input impedance of 1MΩ‖24pF. This shows that $I_{bias,ADC}$ is insufficient to account for the DC level of S_D.

The actual reason for the DC level is the parasitic capacitance of the transistor, as shown in figure 41. Since the capacitance C_p is so small this parasitic capacitance becomes significant, and the voltages over V_{GD} or V_{GS} are sufficient to drive this gate voltage due to the small C_p. The parasitic capacitances C_{GD} and C_{GS} are shown in figure 42. We have $C_{GD} = C_{GS} = 3$pF from appendix B.1. Normally the node connected to V_{cc} (in this case the drain node) would be pulled to ground in the small signal model, but since V_{cc} is duty cycled this is not done in figure 42.

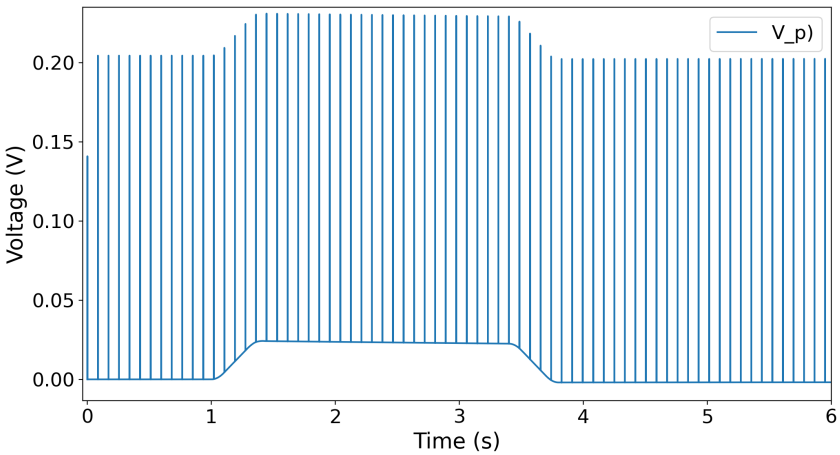

Figure 41: This simulation shows that the voltage at the gate is affected by parasitic capacitance. This explains the DC level we get for S_D. Without the parasitic capacitance, this signal would be smooth, as in figure 4.

An interesting aspect of this is that since V_{out} is a function of C_p (even when $I_p = 0$) we can find C_p through simulation. Using $C_m = 5.6$pF, as in figure 38, and testing different

values for C_p we find that the value that results in $V_{out}(n \cdot t_s) = 1.3\text{V}$ with $C_m = 5.6\text{pF}$ is $C_p = 43\text{pF}$.

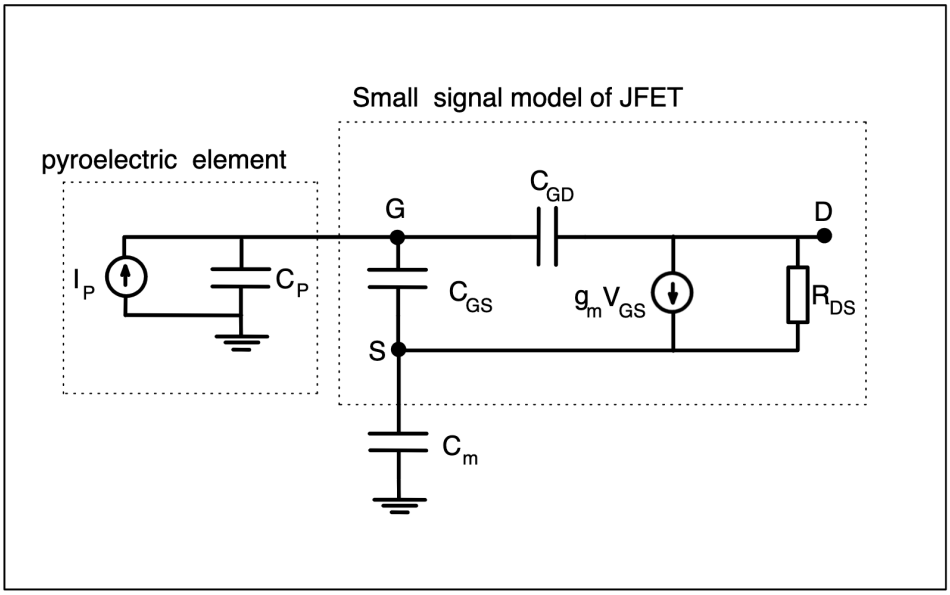

Figure 42: This figure shows a small-signal model for a JFET transistor. When C_p is small, the parasitic capacitances C_{GD} and C_{GS} become relevant. They are what cause the "spikes" seen in figure 41. V_p is the voltage at G (plotted in figure 41), V_{out} is the voltage at S, and V_{cc} (which is duty cycled) is the voltage at D.

Both C_{GD} and C_{GS} contribute to the voltage spikes, but not equally much. The simulation was tested for different values of C_{GD} and C_{GS}, in order to analyze the impact of each of them. When both were set to zero, no spikes appeared. When $C_{GS} = 0$ and $C_{GD} = 3\text{pF}$ the spikes were a third of the full amplitude of what they were in figure 42. When $C_{GS} = 3\text{pF}$ and $C_{GD} = 0$ the spikes were two-thirds of the full amplitude.

10.3 Noise components empirical findings

In this section, we will look at the noise injected into our measurements from a power adapter, from the RPi, and by the digital measurement circuit. Comparing the noise from the digital measurement circuit to the total noise of the measurements we will find that practically all the noise comes from this. Finally, we will see how big $S_{environ}$ is, depending on the environment in which the sensor operates.

10.3.1 Noise from RPi and power supply

Figure 44 shows a measurement out of a pyroelectric element with no person present, and UART lines connected. The RPi is powered by an electrical outlet.

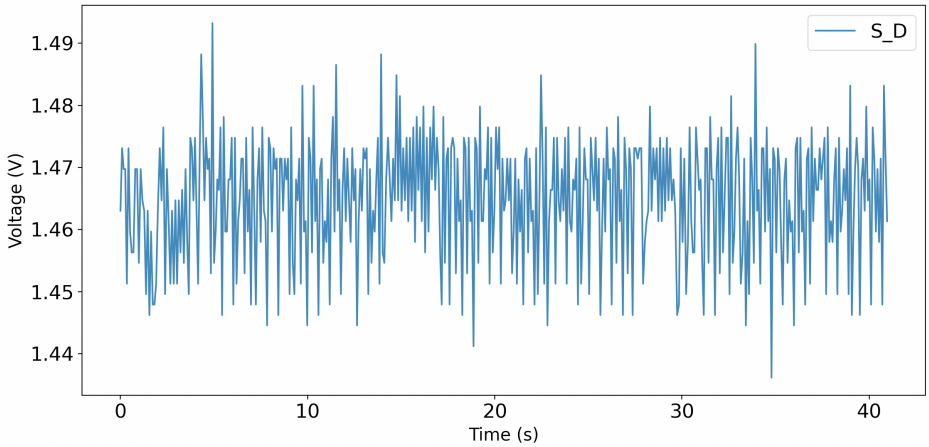

Figure 43: Noise injected by the RPi during measurement. The RPi is powered by an adapter connected to an electrical socket. The standard deviation of the noise is approximately 10mV.

The noise seen in figure 43 mainly stems from the fact that it is connected to the power grid or that the power adapter is noisy, as discussed in section 5.5. This problem can be alleviated by powering the RPi with a power bank. This is done in the measurement shown in figure 44, and it significantly reduces the noise. For all remaining measurements in the thesis, the RPi is powered by a power bank.

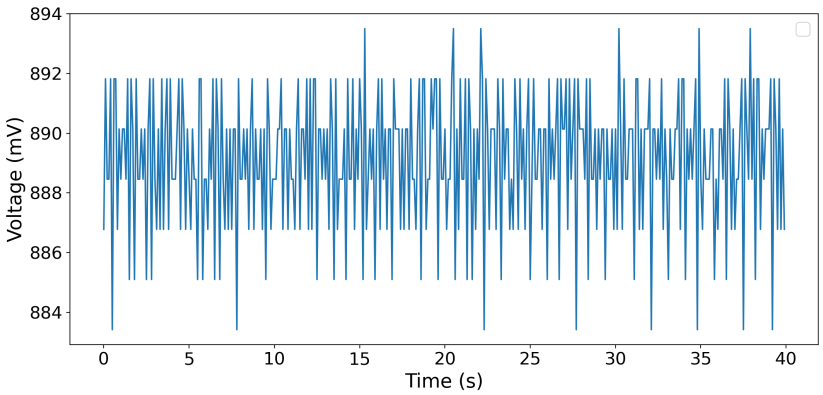

Figure 44: Noise with RPi conncted. It has a standard deviation of approximately 2.2mV. No data is being sent over UART when these measurements are made, so there is no toggling on the lines. Even so, the RPi injects noise.

Figure 45, shows the same measurement as figure 44, the only difference being that the UART lines are disconnected. From this, it is evident that the UART connection constitutes a significant source of noise, as discussed in section 5.5.

Other than for the measurements in figure 45 and 46 we will still have the UART lines connected during measurements. This is because disconnecting the UART lines requires us to use multisampling in between UART-communication, which uses a buffer with a limited size. For continuous measurements, which is a very preferable mode of measurement, we will need to have the UART lines connected.

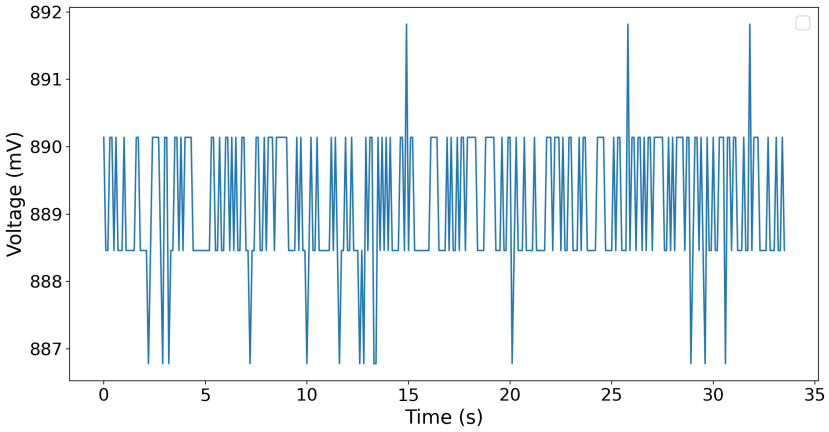

Figure 45: Noise with RPi disconncted. It has a standard deviation of about 0.98mV.

10.3.2 The noise comes from digital circuitry, not the AFE

In order to quantify how much of the noise is from the AFE, and how much is from the digital measurement circuitry, a minimal test setup was made. This minimal test setup consists of a battery that is connected to the ADC through a voltage divider, as shown in figure 46.

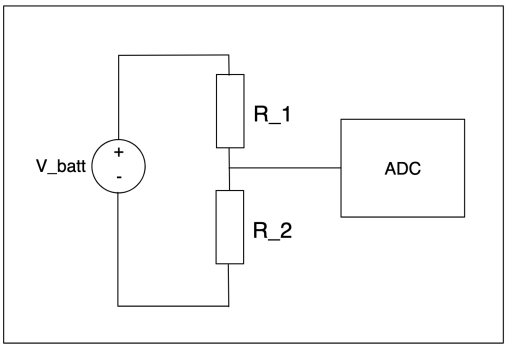

Figure 46: A battery connected to the ADC through a voltage divider. This should provide an almost noiseless reference, allowing us to identify how much of the noise comes from the ADC.

Batteries are practically noiseless voltage sources. [4] At a sampling rate of 10Hz, the thermal noise from the resistors is also negligible. Using (9) we have a noise bandwidth $\Delta f \leq 5$. The total thermal nosie v_n of a resistor $R_1 + R_2 = 3.84\text{k}\Omega + 6.16\text{k}\Omega = 10\text{k}\Omega$ can, inserting into (11), then be expressed as

$$v_n = \sqrt{4k_\text{B}TR\Delta f} \leq \sqrt{4 \cdot 1.38 \cdot 10^{-23}\ \text{m}^2\ \text{kg}\ \text{s}^{-2}\ \text{K}^{-1} \cdot 300K \cdot 10\text{k}\Omega \cdot 5Hz} \approx 28.8\text{nV} \tag{16}$$

which is significantly smaller than the noise observed in figure 47.

Comparing figure 44 and figure 47 we observe that the noise measured with our AFE

connected, is almost identical to the noise measured with a noiseless reference connected. This means that practically all the noise in our system comes from the ADC, rather than the AFE.

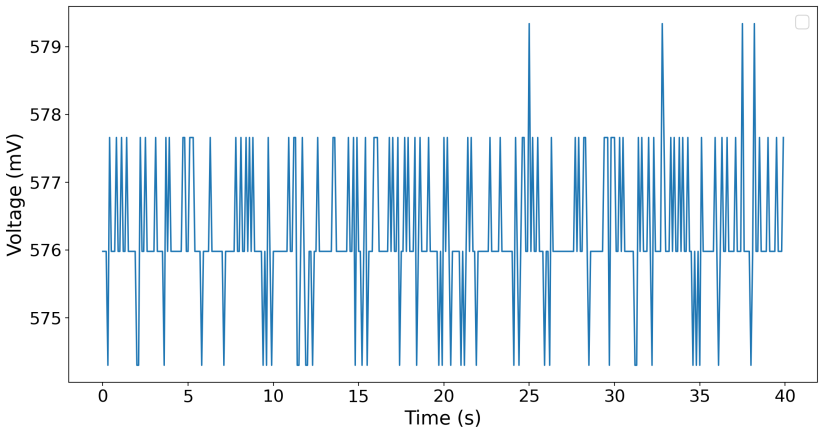

Figure 47: Noise measured from a voltage divider connected to a battery. It has a standard deviation of about 0.97mV. This very clearly illustrates that the noise we see in the measurements is not noise from the AFE, but rather from the digital measurement circuitry.

10.3.3 Measurements of thermal fluctuations in the environment

Figure 48 shows a plot of $S_{environ}$ under two different circumstances.

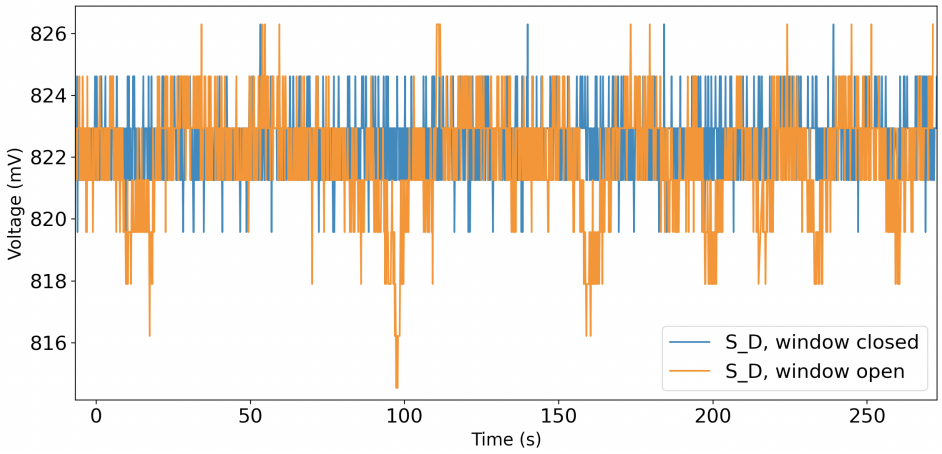

Figure 48: A sensor is situated next to a window. The upper plot shows measurements made with the window closed. The lower plot shows measurements with the window open, resulting in larger thermal fluctuations. The fluctuations with the window closed range between $820 - 826$mV while the fluctuations with the window open range between $814 - 826$mV.

Not only does the measurement made with the window open have a larger standard deviation, but the shape of $S_{environ}$ here is also more similar to what one would expect from S_{human}. However, as we shall see in section 10.6, S_{human} is still significantly bigger than

$S_{environ}$, and the system performs well even when situated next to an open window.

10.4 Example signals at different capacitances

With C_m on the order of magnitude of pF or larger its value is irrelevant to the quality of the signal. Regardless of C_m, the amplitude of the system will be about 20mV and the standard deviation of the noise will be at about 3.5mV. Visually it may seem like the plots have different noise, but this is due to them having a different duration, so the time axis is denser in figure 50 than in 49.

This is as expected from the theoretical discussion.

Figure 49 shows what the signal is like for $C_m = 1$nF, figure 50 for $C_m = 300$pF, figure 51 for $C_m = 100$pF, and figure 52 shows the signal for $C_m = 100$pF. As can be seen from the figures, the main difference between the signals is just the DC offset, rather than a difference in the quality of the signals.

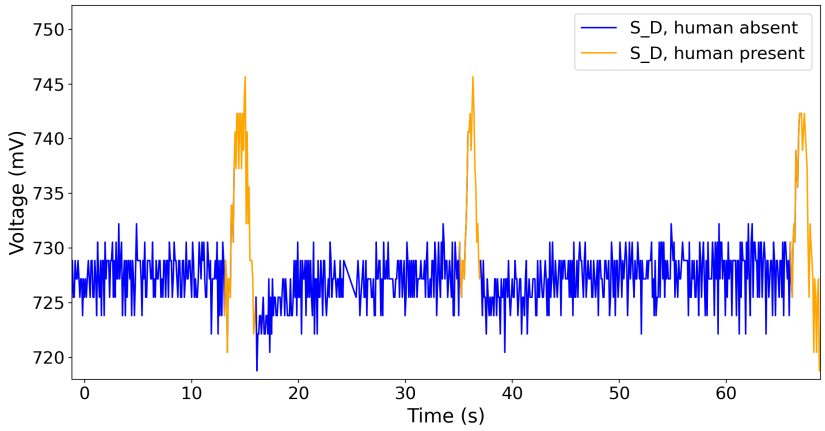

Figure 49: Signal when $C_m = 1$nF.

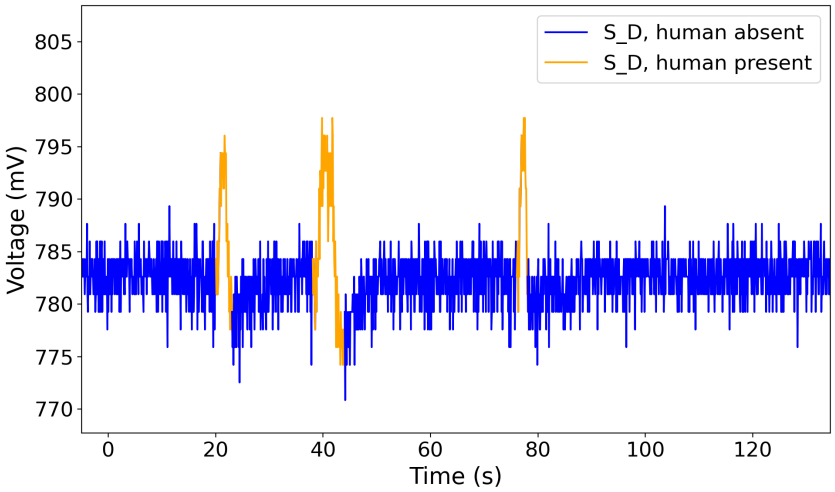

Figure 50: Signal when $C_m = 330$pF.

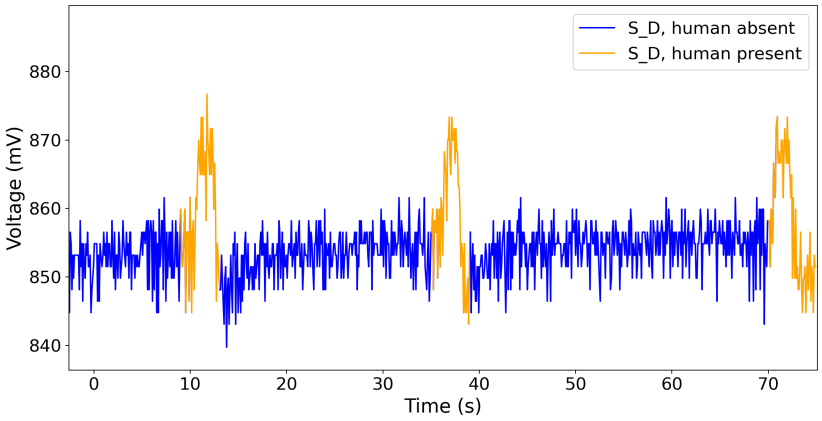

Figure 51: Signal when $C_m = 100$pF.

Figure 52 shows the signal with $C_m = 0pF$. In that case, the capacitance between V_{out} and ground is given purely by $C_{ADC} = 20$pF, the internal capacitance of our ADC. The amplitude of the signal is about 20mV, just as for the other measurements. The noise is somewhat bigger and has a standard deviation of 5.7mV. The reason for this may have to do with component placement. C_m is placed on the breadboard next to the sensor, while C_{ADC} is placed on the other side of jumper wires, inside the ADC. This is a good example of how layout may be crucial to how well the circuit performs. Another reason may be that C_m together with the resistance in the transistor may constitute a filter, and that for $C_m = 0$ the circuit is less resilient to digital switching noise. The increase in noise does not come from the AFE. This was established in section 10.3.2.

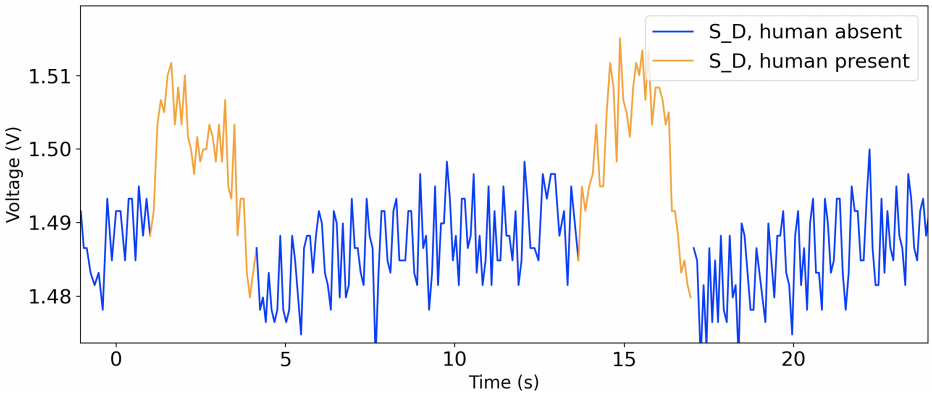

Figure 52: Signal when $C_m = 0$pF, resulting in a total capacitance of $C_m||C_{ADC} = 0\text{pF}||20\text{pF} = 20$pF between V_{out} and gnd. The noise is most likely not caused by the fact that 20pF is a small capacitance, but rather is due to the placement of the capacitor relative to the sensor element.

With the particular ADC used in this thesis, in which we have $C_{ADC} = 20$pF, the power consumption of the measurement shown in figure 52 is the lowest power consumption we can achieve. Modifying (14) to also take into account C_{ADC} and inserting into it we obtain a power consumption of

$$P = (C_m||C_{ADC}) \cdot V_{out}^2 (n \cdot t_s) \cdot f_{sample} \approx 20\text{pF} \cdot (1.5\text{V})^2 \cdot 10\text{Hz} = 450\text{pW} \qquad (17)$$

where $C_m = 0$, $C_{ADC} = 20\text{pF}$, $V_{out}(n \cdot t_s) \approx 1.5V$, and $f_{sample} = 10\text{Hz}$.[14]

10.5 A brief note on the signal quality of a resistive circuit

As mentioned in section 6 it is possible to duty-cycle the resistive AFE (seen on the left side of figure 15). While that particular topology is not the topic of this thesis, it will still be briefly explored below.

Figure 53 shows a measurement made with the resistive AFE, with a value of $R_{bias} = 47\text{k}\Omega$. Other than replacing C_m with R_{bias} every aspect of the measurements made in this section is the same as in section 10.4.

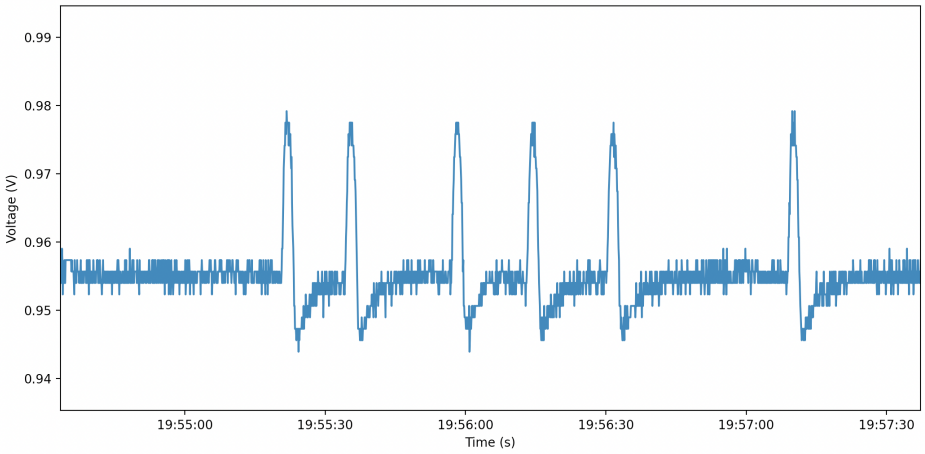

Figure 53: A signal obtained by connecting a resistive AFE (as shown on the left side of figure 15). For this measurement $R_{bias} = 47\text{k}\Omega$. The measurement is still made the same way, including duty cycling. Six peaks indicating motion are clearly visible.

The signal in figure 53 shows six very apparent peaks indicating motion. This suggests that a resistive AFE also works well, even when it is duty cycled.

The power consumption by R_{bias} is approximately

$$P_{R_{\text{bias}}} = \frac{V_{\text{out}}^2}{R_{\text{bias}}} \cdot \text{ duty } = \frac{V_{\text{out}}^2}{R_{\text{bias}}} \cdot \frac{t_{on}}{t_s} \approx \frac{(1\text{ V})^2}{47\text{ k}\Omega} \cdot \frac{15\ \mu\text{s}}{0.1\text{ s}} \approx 3.2\text{nW} \tag{18}$$

which is a significant reduction from what it would be if the AFE was not duty-cycled. The values $t_{on} = 15\ \mu$s and $t_s = 0.1$ s are representative of what they were for the measurement shown in figure 53, and the value of $R_{bias} = 47\text{k}\Omega$ was chosen for the measurement since that is a very typical value of a biasing resistor in PIR systems. [12].

One should keep in mind that the impedance between source and ground still contains a capacitive component, C_{ADC}. This means that one should consider that the impedance is $Z_{bias} = R_{bias}||C_{ADC}$. This means that the power consumption of the resistive component

[14] We choose $f_{sample} = 10\text{Hz}$ because it was found empirically to result in correct detections. The prototype described in section 11.1.1 was tested for different values of f_{sample}. At 8Hz some misdetections occurred. $f_{sample} = 9\text{Hz}$ did not result in any misdetections, but $f_{sample} = 10\text{Hz}$ was chosen as it is a round number better suited for calculations, which also provides some margin from the sampling rate at which the system has failures.

calculated in (18) will come on top of the power consumption we have in the capacitive component calculated in (17). As $R_{bias} \to \infty$, $Z_{bias} \to C_{ADC}$, and the AFE becomes the capacitive variation that is used for the rest of the thesis, with $C_m = 0$. The advantage of having $R_{bias} \to \infty$ is that $P_{R_{\text{bias}}} \to 0$, and we are left with only the power consumption of C_{ADC}. The disadvantage is that the noise increases. The signal in figure 53 is less noisy than what the capacitive system is. This is likely because the impedance Z_{bias} acts as a filter, making the measurements more resistant to noise from the digital circuitry. However, the noise will only increase up to what we have for the capacitive system in which $C_m = 0$. As we shall see in the next section, the system performs well even when Z_{bias} has no resistive component, so there is no reason to trade the slight noise reduction against increased power consumption.

10.6 System performance for different algorithm parameters

Figure 54 shows an example of how the algorithm described in section 4 performs for different parameters. For that figure we have $i = 3$, $j = 6$ and $offset = 10\text{mV}$. The program pictured in figure 54 was made in order to test the impact of different parameters of i, j and $offset$. The method for averaging is batch averaging. It shows a comparison between two different signals. The left signal is generated by the test rig and should result in detections. If there are not six detections in the left plot for our particular set of parameters, we would have missed detections. The right is noise, resulting from the sensor being left alone for 15 minutes next to an open window, with no motion near it. If there are any detections in the right-hand plot, these would count as misdetections.

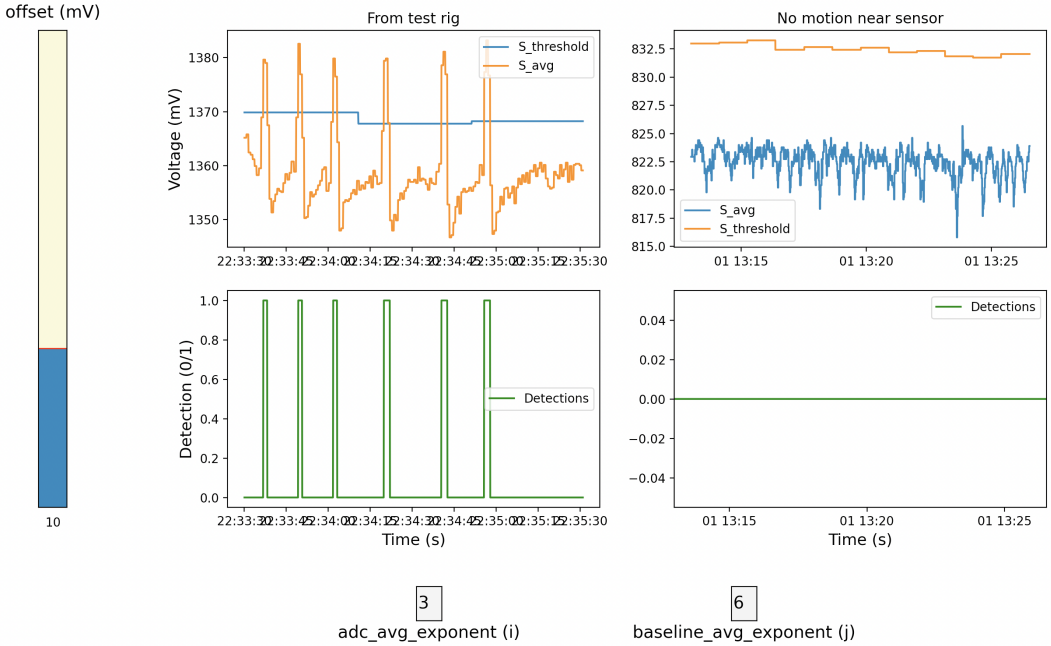

Figure 54: An example of how the algorithm performs for a particular set of parameters. Here $i = 3$, $j = 6$ and $offset = 10\text{mV}$. The left plot is showing a signal generated by the test rig, equivalent to a person passing the sensor element 6 times. The right shows 20 minutes of noise, for which there should be no detection.

For indoor motion detection, the sensor would typically experience less environmental

temperature variation than a sensor next to an open window does. Regardless, this is a good stress test for the system. Because of that, all the "reference noise" in this section is generated from a sensor next to an open window. The noise injected by the test rig (powered by a power bank, with UART connected, since the measurements are running continuously) is present in the signal. This noise would not be present in a sensor that is not connected to a test rig. Because the noise in this test is bigger than it would be in most circumstances, the estimates of the performance provided in this section are conservative estimates. Still, the sensor performs without error in all tests, if one chooses the right parameters, as shown in table 1 and 2.

As one can see from figure 54 S_{human} is significantly bigger than $S_{environ}$. When there is no motion near the sensor, S_{avg} seems to run no risk of crossing $S_{threshold}$ for sensibly chosen parameters of the algorithm. As seen from table 1 a range of $offset = 3 - 15$mV will result in no misdetection nor missed detections.

The tests that the tables in this section are based on were done for three different values of C_m (330pF, $C_m = 5.6$pF and $C_m = 0$), and the values in the tables are representative for all these values of C_m. The sampling rate for all the tests was chosen to be 10Hz. In all the tests the signal used to test for misdetections (with no motion near the sensor) ran for at least 15 minutes.

$offset$ (mV)	misdetection	missed detections
$3 - 15$	0	0
$15 - 19$	0	$1 - 3$
20	0	all
2	$5 - 7$	0
1.5	$12 - 19$	0
1	all	0

Table 1: Misdetections and missed detections for different values of $offset$, with $i = 3$ and $j = 4$. The total amount of possible detections for each of the tests was in the range of $5 - 7$ detections.

Table 2 shows how the system performs for an $offset = 10$mV, and different values of i and j. There were no misdetections during this test, so that is not included in the table. A value of 3 or 4 for i and j gives the least misdetections. This makes sense since that would mean that the time over which S_{avg} is sampled is around $2^3/10\text{Hz} \approx 1$s, which is slightly smaller than the duration of a signal induced by motion. If it were averaged over a much larger time the motion signal would be averaged away, as one can see happens for $i = 6$. If j is too small $S_{threshold}$ would follow S_{avg} too quickly, and S_{avg} would not have time to increase above it when motion occurs.

i	j	missed detections
1	$1-2$	all
1	$4-3$	$0-2$
1	$4-6$	0
2	1	all
2	2	$0-2$
2	$3-6$	0
3	$1-6$	0
4	$1-6$	0
5	$1-6$	$1-3$
6	$1-6$	all

Table 2: Missed detections for $offset = 10\text{mV}$ and various values of i and j. The same signals were used for this test as for table 1.

11 Implementation of a full IoT system

Figure 55 shows a sensor prototype molded in an epoxy mixture for robustness. The system in figure 55 contains the entirety of the sensor node, including the antenna, the battery, microcontrollers and of course the sensor element itself. This was mounted in the ceiling of an office space and sent a detection to the cloud platform whenever someone walked beneath it. The results from the test with this prototype are discussed in section 11.1.

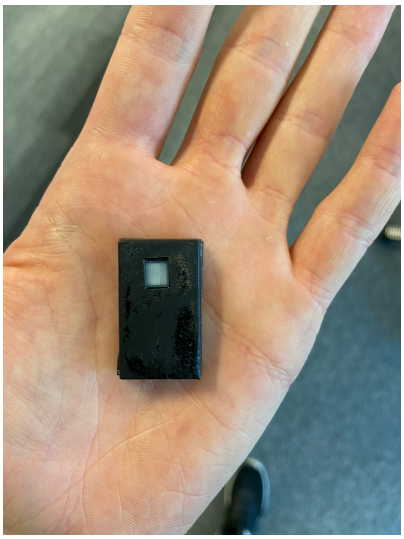

Figure 55: A picture of a complete sensor prototype.

The prototype sensor fits into the solution that Disruptive Technologies (DT) provides as illustrated by figure 56. The prototype sensor contains firmware that allows it to process detections (and a hardware implementation of the algorithm described in section 4.3) as well as send the detections to a gateway called a cloud connector. This gateway then relays this message to the cloud, which is DTs backend for handling sensor data. This data can then be viewed in an end application, such as for instance DT-Studio which is what DT provides out of the box.

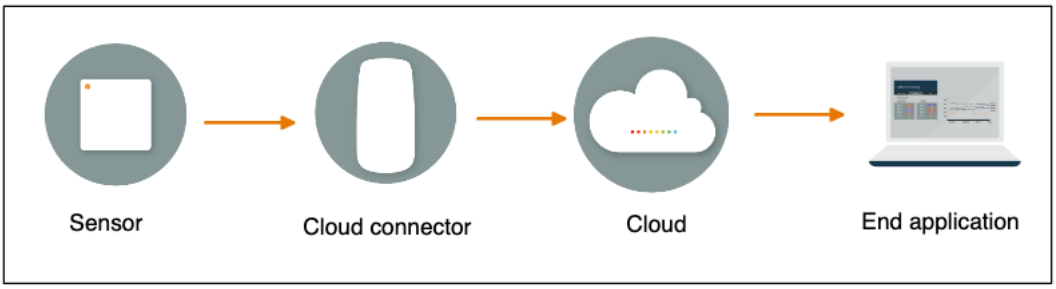

Figure 56: An illustration of where the sensor prototype fits into the architecture provided by Disruptive Technologies. The prototype sensor sends a message to the cloud connector when it detects motion, which is a gateway that further relays the message to the cloud. The cloud provides a backend for whichever end application you might wish to integrate it with. DT also provides a front end that is called DT-Studio. The icons in this figure are provided by DT, and used with their permission. They are the only part of any figure not made by the author.

A simplified schematic view of what the prototype sensor contains is shown in figure 57. The complete prototype is shown in figure 55. The AFE is the analog front end proposed in section 6. The DT-die is a custom low-energy IC created by DT for measuring sensor elements and contains the ADC as well as the hardware implementation of the algorithm for motion detection. When a detection occurs the DT-die will wake up a microcontroller. The microcontroller contains a radio that will then send a message to the cloud connector.

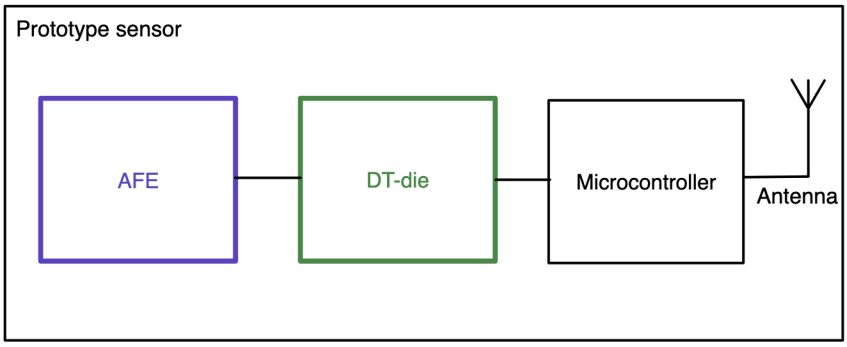

Figure 57: A simplified view of the contents of the prototype sensor.

11.1 Test of prototype

Several implementations of the prototype were made. The one shown in figure 55 is a very early prototype. The advantage of it being an early prototype is that it is possible to test it for a long duration, as described in section 11.1.1. Another prototype, which has $C_m = 0$ and a sampling rate of 10Hz, was also made at a late point. That prototype was mounted in the ceiling of an office space and observed for one hour. During that time it had no misdetections nor missed detections. In this period, it made a total of 30 detections.

11.1.1 Test of first complete system prototype

A prototype of the sensor is described in the previous section. It was mounted in the ceiling of an office space and sent detections to Disruptive Technologies' cloud platform whenever someone walked underneath it. The prototype gives an idea of how a finished product integrating the sensor might work, as well as what sort of challenges one might need to consider for this.

The prototype consistently sent correct detections during the three days in which the author was present to observe the times at which people passed under it.

After this one can only make qualitative assessments regarding whether the detections are correct, as there was no reference sensor to compare the detections with. The sensor appears to only be firing at sensible times, only during office hours and with higher intensity during break hours, for about 1.5 months. After this, there are several erroneous detections outside of office hours, with increasing frequency until the sensor reaches a complete breakdown after two months.

As the sensor was a first prototype it had several flaws. Firstly it was configured to have a sampling frequency of 100Hz, which is much more than what is required for motion detection.

Secondly, it sent way more data than what is strictly necessary. Thirdly it still contained the capacitors $C_{i,1}$ and $C_{i,2}$. The combination of these three things is most likely what caused it to fail. Additionally, the battery used for the prototype is CR1216 [8], which has a nominal capacity of 25mAh and a diameter of 12.5mm and a height of 1.6 mm. Alternatively, a better choice for this sensor could be to use BR1225 [5] which has double the capacity and could still fit within the dimensions of the prototype.

The sensor was configured to send each time it detects movement, regardless of the time interval between the movements. The way that this is normally handled by PIR sensors is to have a timeout. In that case, when motion is detected the sensor sets its status as "person present" and a countdown is started. Whenever motion is detected within this interval the countdown is reset. If the countdown reaches zero the status is changed to "no person present". Depending on the placement of the sensor and the chosen timeout, sending only "person present/person not present" rather than once for each "motion detected" can drastically reduce the amount of data sent.

Taking into consideration the flaws of the first prototype, the fact that it worked well for 1.5 months is a promising result.

11.2 Long time test with reference

A setup consisting of a prototype sensor, a reference sensor, and an RPi is shown in figure 58. This setup was mounted in the ceiling of an office space, and tested for a month.

The reference sensor is a breakout board of type HC-SR501 [11] with time delay adjustment set to minimal (5s), and range set to 3m. The RPi is responsible for reading the data from both the prototype sensor and the reference sensor, timestamping them and writing them to a file. A custom program was written to interface it with the prototype sensor over UART, allowing it not only to read whether the DT-die registers a detection but also to obtain the raw measurement data from the ADC. In order for this to work the prototype

sensor is running a debug image, rather than the low-energy firmware image that will be used in the final version. The RPi is also programmed to send both the detections from the reference sensor and the prototype sensor to the cloud so that it is available to view in DT-studio (which is DTs web app for viewing sensor data).

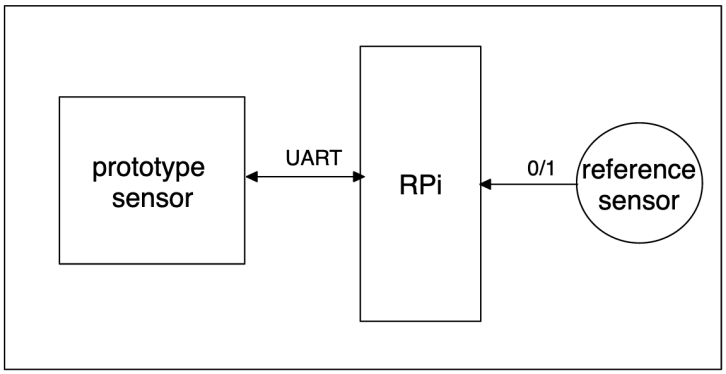

Figure 58: A setup utilizing a RPi to collect data on the behavior of the sensor. The reference sensor used is of type HC-SR501 [11]. The prototype sensor runs a firmware image that allows it to communicate with the RPi over UART.

The big drawback of this test is that the reference sensor is a lot less reliable than having a full test rig. In fact, the reference sensor appeared to perform less reliably than the prototype sensor itself. The reference sensor was triggered multiple times during the middle of the night when the office was closed, whereas the prototype sensor did not have any such detections. The reference sensor also has a wider field of view, which means that in some cases it will pick up motion that the prototype sensor does not detect. Both the prototype sensor and the reference sensor show an increased number of detections during office hours, especially during lunch hours.

The fact that the reference is not entirely reliable diminishes the value of an analysis showing exact numbers for the correlation between the data from the reference and the prototype sensor. Regardless, this test can still be seen as having a qualitative value. HC-SR501 is a commonly used sensor for motion detection, and the above assessments seem to indicate that the prototype sensor has comparatively more reliable detections.

12 Further work

There are many possibilities for future work. Here we will discuss some of them. The possibilities discussed are using a different ADC, exploring new applications and integrations, testing other components in the system, and expanding upon the simulation.

12.1 Use a different ADC

There are several reasons that the chosen ADC was used in this thesis. The ADC is a custom design by DT, created for low-energy sensing in an IoT node. This means it has the advantage of already being integrated into a platform on which it is possible to build a full system, as was done in section 11. It also means that it is designed for very low

energy consumption. Many other ADCs consume a considerable amount of energy and would therefore be less suited for a low-energy pyroelectric motion detection system.

However, multiple drawbacks stem from the fact that this ADC was originally designed for a different sensor system. The internal biasing current of the ADC, $I_{bias,ADC}$, should ideally be zero for this system, but that is not possible on the platform used. The internal capacitance of the ADC should ideally be zero, but it is 20pF. The dynamic range of the ADC is not fitted to the range of the signal[15], so we lose some of the signal quality.

Using an ADC that does not have these limits and is custom-tailored to this specific use case, would significantly lower the possible power consumption of the system, and improve the quality of measurements. Currently, the ADC is the bottleneck of the system, by a good margin, and would be the best place to start when improving the system further.

12.2 Eplore new applications and integrations

The focus of this thesis has been on using the sensor for presence detection in a room. However, there are many other possible use cases. One could use the sensor as a non-contact button, for a desk occupancy system, or as a wakeup for more advanced and power-hungry measurement systems.

One could also consider integrating the measurement method into more complex systems, such as using it as a component in a communication system. Integrating the sensor into a system that has an energy harvester could potentially make a system that never runs out of power.

12.2.1 Non-contact button preseeing

PIR motion detection is widely used for non-contact buttons in wired systems such as sinks or hand dryers. Those systems do not require low energy consumption. However, if one wants a non-contact button for a battery-powered system it needs to be low-energy. The proposed system is especially suited for this, and it has an even clearer signal than one has for normal motion detection, due to the large thermal flux of a hand close to the sensor element.

12.2.2 Desk occupation system

Low-energy IoT desk occupancy sensors exist, such as the one from Disruptive Technologies. [30] However, the current solution comes with the drawback of a relatively long latency of 5-10 minutes. Integrating a PIR sensor into this system would make the responsiveness practically immediate. The existing system would provide stability to the sensing that is not available with only PIR sensing, so combining PIR sensing with the existing system would be advantageous.

[15] Only to the degree which can be achieved through some calibration, which is limited.

12.2.3 Wakeup for more advanced measurement systems

The information obtainable through a PIR sensor is highly limited. It is possible to know whether there is any motion close to the sensor element, but not which direction the movement has, or any further information regarding the object sensed.[16]

More advanced sensors, such as thermal cameras generally require more power but also have a broader range of capabilities. A thermal camera may be used for people counting if placed in a doorway. It might also provide a better overview of how rooms are used. Existing solutions for this, such as [6], could be made smaller and achieve longer battery life if they were mostly asleep, and only woken up when a PIR sensor detects motion in the vicinity of the sensor.

A PIR sensor could also act as the trigger for waking up a photo trap. This could enable small long lasting motion-triggered cameras for instance for animal photography.

12.2.4 Low energy communication system

Pyroelectric elements are employed in several communication systems. By modulating laser pulses onto the element one can transfer bits. There exist small sensors with a need for low-energy communication. One could explore the possibility of using the proposed pyroelectric measurement system for this.

There are significant differences between motion detection and communication systems, so there is a big probability that the measurement circuit would not be suited for communication. Nevertheless, it might be worth exploring.

12.3 Test other components

The pyroelectric element and transistor that were used in this thesis provided good results. It might nevertheless be interesting to characterize and analyze the impact that the choice of components has on the performance of the system. Practical concerns regarding substituting the transistor are the subject of appendix C. Testing other pyroelectric elements would also be interesting, especially if one expands upon the simulation, as will be discussed in the next section.

12.4 Expand upon the simulation

The simulation presented in this thesis starts with some assumptions regarding the pyroelectric current I_p, and an approximate value for this is fed into the simulation. This is due to limited access to information regarding the physical nature of the pyroelectric element, which is not publicly available. However, if one knows all the physical properties of the pyroelectric element, it is possible to simulate how it heats up in the presence of the thermal flux of a human.[17] This, in turn, allows one to exactly simulate the pyroelectric current I_p, which can be fed into the simulation presented in section 9.

[16] Unless one uses advanced PIR-measuring methods such as the ones presented in [10]

[17] By using simulation software such as COMSOL

13 Conclusion

The goal of this thesis is to explore the degree to which one can reduce the energy consumed by a passive infrared (PIR) pyroelectric sensing system. The system proposed in this thesis achieved a power consumption of 450pW, without any loss in the quality of detections as compared to existing PIR solutions. This may be considered a significant reduction from existing low-energy systems for PIR detection, which consume about 6μW.[12] The performance of the system was demonstrated by a test rig, simulation and a prototype.

The method with which this reduction in power consumption was achieved was to duty cycle the system. Typically, in PIR sensing, the pyroelectric element is connected to a source follower. That AFE was shown to work, even when duty-cycling. However, an AFE in which the biasing resistor of the source follower is replaced with a capacitor, was shown to have a smaller power consumption.

During the testing of the system, not a single misdetection nor missed detection was observed. This applies to the measurements in the test rig, the simulation, and the prototype.

The construction of a test rig was essential to prove that the circuit behaves as expected and for obtaining consistency across experiments with different components and variables. The test rig was calibrated to provide identical heat radiation onto the sensor element as a person passing under a ceiling-mounted sensor. When applying an algorithm based on moving thresholding to the signal obtained in the test rig, the system consistently made only correct detections.

The functionality of the system was further verified by simulation. The simulation agreed with the measurements. Additionally, it revealed that the parasitic capacitances of the transistor affected the DC level of the output of the AFE. Without the simulation, the results would be limited by practical measurement considerations, such as the resolution of the ADC or issues with the digital circuitry.

Indeed, the digital measurement circuitry, rather than the AFE, turned out to be the main limiting factor of the system. The measurement noise is shown to be practically only from the digital circuitry. Additionally, the limiting factor for reducing power consumption is the fact that our ADC has an internal capacitance between its input and ground. The advantage of the chosen ADC is that it is integrated into a platform for low-energy IoT sensing systems, allowing for constructing a full IoT system by only connecting an AFE to it. Such a system was created and demonstrated to perform reliably.

The fact that such a low-energy implementation of a PIR measurement system is possible opens up new opportunities for IoT applications, as exemplified by the prototype.

14 Acknowledgements

I thank my advisors Pål Øyvind Reichelt and Dag Roar Hjelme, for all their help. Pål Øyvind is my advisor from Disruptive Technologies, and I am grateful to him for all his technical guidance. I am grateful that he replied to questions quickly and well, often on the same day, sometimes even outside of working hours. I am grateful to him for inspiring me to take on this project, and for suggesting that combining the DT-die and a PIR element might be a good idea. I am grateful for the editorial advice of both my advisors and Dag Roar Hjelme for answering logistical questions regarding NTNU and writing a master's thesis. I am also grateful to Dag for introducing me to Cuong Phu Le. And to Coung Phu Le for being very helpful in answering practical questions regarding modeling a pyroelectric element. I am also grateful to Gunnar Bolme for helping me with difficult soldering tasks, without which the disassembly would not be possible, and to all my colleagues at DT for aiding me with miscellaneous practical problems. The author is also grateful to all other contributions provided by Disruptive Technologies (as further detailed in appendix A.3) and that they were willing to let me write my master thesis for them.

References

[1] *1880682.Pdf*. URL: https://www.farnell.com/datasheets/1880682.pdf (visited on 08/05/2023).

[2] Giuseppe Franco Bassani, Gerald L. Liedl and Peter Wyder. *Encyclopedia of Condensed Matter Physics*. 1st ed. Amsterdam Boston: Elsevier, 2005. ISBN: 978-0-12-369401-0.

[3] 'BC517 - NPN Darlington Transistor'. In: (2005).

[4] C.K. Boggs, A.D. Doak and F.L. Walls. 'Measurement of Voltage Noise in Chemical Batteries'. In: *Proceedings of the 1995 IEEE International Frequency Control Symposium (49th Annual Symposium)*. Proceedings of the 1995 IEEE International Frequency Control Symposium (49th Annual Symposium). May 1995, pp. 367–373. DOI: 10.1109/FREQ.1995.483923.

[5] *Br1225-2019.Pdf*. URL: https://data.energizer.com/pdfs/br1225-2019.pdf (visited on 10/12/2022).

[6] *Butlr_datasheet.Pdf*. URL: https://query.prod.cms.rt.microsoft.com/cms/api/am/binary/RWZb7m (visited on 24/06/2023).

[7] Tony Chan Carusone et al. *Analog Integrated Circuit Design*. 2nd ed. Hoboken, NJ: John Wiley & Sons, 2012. 794 pp. ISBN: 978-0-470-77010-8.

[8] *Cr1216_datasheet.Pdf*. URL: https://industrial.panasonic.com/cdbs/www-data/pdf2/AAA4000/AAA4000C277.pdf (visited on 22/11/2022).

[9] 'DS18B20 - Programmable Resolution 1-Wire Digital Thermometer'. In: ().

[10] Jian-Shuen Fang et al. 'Path-Dependent Human Identification Using a Pyroelectric Infrared Sensor and Fresnel Lens Arrays'. In: *Optics express* 14 (1st Feb. 2006), pp. 609–24. DOI: 10.1364/OPEX.14.000609.

[11] *HC-SR501 Datasheet*. URL: https://www.mpja.com/download/31227sc.pdf (visited on 10/12/2022).

[12] *How to Bias PIR Sensors to Prolong Battery Life in Wireless Motion Detectors - Analog - Technical Articles - TI E2E Support Forums*. URL: https://e2e.ti.com/blogs_/b/analogwire/posts/how-to-bias-pir-sensors-to-prolong-battery-life-in-wireless-motion-detectors (visited on 12/09/2022).

[13] *JQC-3FF-S-Z.Pdf*. URL: https://denkovi.com/Documents/JQC-3FF-S-Z.pdf (visited on 25/05/2023).

[14] Benedikt Andreas Mithassel. 'Reduction of Energy Consumption in Pyroelectric Motion Detection'. In: ().

[15] *Msds_apc_pzt.Pdf*. URL: https://www.americanpiezo.com/images/stories/content_images/pdf/msds_apc_pzt.pdf (visited on 02/02/2023).

[16] H. Nyquist. 'Thermal Agitation of Electric Charge in Conductors'. In: *Physical Review* 32.1 (1st July 1928), pp. 110–113. ISSN: 0031-899X. DOI: 10.1103/PhysRev.32.110. URL: https://link.aps.org/doi/10.1103/PhysRev.32.110 (visited on 23/05/2023).

[17] *PL-N823-01*. URL: https://www.kemet.com/en/us/sensors/product/PL-N823-01.html (visited on 20/10/2022).

[18] Yuriy Poplavko and Yuriy Yakymenko. *Functional Dielectrics for Electronics: Fundamentals of Conversion Properties*. Woodhead Publishing Series in Electronic and Optical Materials. Duxford, United Kingdom ; Cambridge, MA: Woodhead Publishing, an imprint of Elsevier, 2020. 294 pp. ISBN: 978-0-12-818835-4.

[19] Akshay Potnuru and Yonas Tadesse. 'Characterization of Pyroelectric Materials for Energy Harvesting from Human Body'. In: *Integrated Ferroelectrics* 150.1 (2nd Jan. 2014), pp. 23–50. ISSN: 1058-4587, 1607-8489. DOI: 10.1080/10584587.2014.873319. URL: https://www.tandfonline.com/doi/full/10.1080/10584587.2014.873319 (visited on 01/02/2023).

[20] V.P. Pyatti. 'An Exact Expression for the Noise Voltage across a Resistor Shunted by a Capacitor'. In: *IEEE Transactions on Circuits and Systems I: Fundamental Theory and Applications* 39.12 (Dec. 1992), pp. 1027–1029. ISSN: 10577122. DOI: 10.1109/81.207729. URL: http://ieeexplore.ieee.org/document/207729/ (visited on 27/06/2023).

[21] C. R. Bowen et al. 'Pyroelectric Materials and Devices for Energy Harvesting Applications'. In: *Energy & Environmental Science* 7.12 (2014), pp. 3836–3856. DOI: 10.1039/C4EE01759E. URL: https://pubs.rsc.org/en/content/articlelanding/2014/ee/c4ee01759e (visited on 25/11/2022).

[22] *Sensors & IoT Infrastructure — Disruptive Technologies*. URL: https://www.disruptive-technologies.com (visited on 19/11/2022).

[23] *Stepd-01-Data-Sheet-1143075.Pdf*. URL: https://www.mouser.com/datasheet/2/758/stepd-01-data-sheet-1143075.pdf (visited on 05/06/2023).

[24] Felisa Sze and Brendan Hanrahan. 'Pyroelectric Energy Harvesting: Model and Experiments'. In: (2016).

[25] *TF412S*. URL: https://www.onsemi.com/products/discrete-power-modules/jfets/tf412s#technical-documentation (visited on 27/04/2023).

[26] *Tf412s-d.Pdf*. URL: https://www.onsemi.com/pdf/datasheet/tf412s-d.pdf (visited on 27/04/2023).

[27] *The Future of the IoT (Batteries Not Required)*. MIT News — Massachusetts Institute of Technology. URL: https://news.mit.edu/2021/future-iot-batteries-not-required-0521 (visited on 13/12/2022).

[28] *Uln2001.Pdf*. URL: https://www.st.com/resource/en/datasheet/uln2001.pdf (visited on 05/06/2023).

[29] David White. 'The Noise Bandwidth of Sampled Data Systems'. In: *Instrumentation and Measurement, IEEE Transactions on* 38 (1st Jan. 1990), pp. 1036–1043. DOI: 10.1109/19.46397.

[30] *Wireless Desk Occupancy Sensor - Product Datasheet 1.0. (1).Pdf*. URL: https://www.disruptive-technologies.com/hubfs/Wireless%20Desk%20Occupancy%20Sensor%20-%C2%A0Product%20Datasheet%201.0.%20(1).pdf (visited on 24/06/2023).

[31] *Wireless Motion Sensor - Product Datasheet 1.0.Pdf*. URL: https://www.disruptive-technologies.com/hubfs/Product%20specification%20sheets/Wireless%20Motion%20Sensor%20-%C2%A0Product%20Datasheet%201.0.pdf (visited on 19/11/2022).

A Some notes regarding the writing of this thesis

A.1 Generative AI did not write any part of this thesis

As artificial intelligence becomes more advanced and prevalent in academic writing, clarity regarding its use becomes important. At the time of writing, generative tools such as chat-GPT (with models up to GPT-4) exist and masters students are allowed to use them for their thesis. Despite this, the thesis in its entirety is written by the author and not an AI. Grammarly, which is another writing tool, was used. However it was only used for correcting grammar, and the sentence rewriting functionality (that one could consider generative) was not used.

Chat-GPT was used to assist with some parts of the code for processing and plotting the data, but not for writing. It has also been used for inspiration in debugging some issues in the electrical circuitry.

A.2 This thesis is a continuation of a project thesis

This thesis is a master's thesis for the course TFE4940 at NTNU (Norwegian University of Science and Technology). Prior to the master thesis students write a project thesis, such as [14]. This thesis is a continuation of [14], which is not publically available, but rather an assignment handed in internally to NTNU. Reuse of parts of the project thesis in the master thesis is allowed, and students are encouraged to be transparent about this. As such, an overview of how this thesis builds on [14] is provided below.

Section 1.1 is practically unchanged from the project thesis, since the motivation for creating a low-energy motion detection system is the same now as it was then. Section 2.1 and 2.4 are also found in the project thesis.

Much of section 3 is similar to the project thesis. The same detection algorithm was used in the project thesis, but still almost all of section 4 is new and not found in [14].

None of section 5 is found in the project thesis. Section 6 bears some semblance to the project thesis, since it is the same measurement circuit.

Section 7 is unique to this thesis, and no test rig was used for the project thesis.

The sensor modification from section 8 was illustrated in an appendix in the project thesis, but not carried out completely, so it is partly new to this thesis.

Section 9 is unique to this thesis, as no simulation was done in the project thesis. The discussion of signal quality in section 10 is also unique to this thesis.

The implementation of the IoT system in section 11 is very similar to that in the project thesis. The main difference is that in the project thesis, the sensor element modification was not done, so there was no capacitor C_m, only the 2nF capacitors $C_{i,1}$ and $C_{i,2}$ down to ground from drain and source respectively. This means the system from the project thesis had a much higher power consumption.

Some of the suggestions for further work are the same here as in the project thesis. Specifically exploring different sensor elements, using energy harvesting, and using it to wake up a thermal camera. The conclusion is also unique to this thesis and shares practically

no sentences with the conclusion of the project thesis.

In short, the main improvements from the project thesis are that in the project thesis, there was no test rig, no simulation, no discussion of the Peltier equivalent model, no discussion of noise and SNR, and no discussion of the impact of different capacitances C_m on the signal.

A.3 This thesis was written for a company called Disruptive Technologies

The thesis is written for Disruptive Technologies (DT). As they have provided important contributions it becomes relevant to clarify what is the work of the author, and what is done by DT.

Combining the DT-die with the "capsense measurement system" of the DT-die (referred to as the ADC in the thesis) is the idea of disruptive technologies. More specifically Pål Øyvind Reichelt. However, how this is done, and the choice of the AFE, is the idea of the author. The DT-die is a low-energy proprietary IC created by DT.

The research in section 2, 3, and 5, is entirely the work of the author.

The choice of algorithm, presented in section 4 comes from the fact that this is an algorithm that DT has already implemented in hardware, and it happens to coincide with the algorithm for a different sensor system already created by DT.

The construction of a test rig in section 7 is entirely the work of the author. However, it was the idea of DT to use a Peltier element. Work on the test rig was also done by the author as a part-time job prior to the thesis, in order to test the existing PIR sensor of DT. Additionally, it is worth noting that the firmware that allows interaction with the DT-die over UART was written by disruptive technologies. The software on the side of the RPi is written by the author but to some degree inspired by an existing Jupyter notebook written by DT.

The disassembly of the sensor in section 8 is done by the author. However, connecting the disassembled sensor to the DT-die, as done for the prototype in section 11, required precise soldering with which DT helped.

The simulation is the work of the author. However, DT helped with the calculation of $I_{bias,ADC}$, which is based on the internal workings of the DT-die.

All measurements and plots are the work of the author.

The implementation of the full IoT prototype, presented in section 11 would not be possible without DT. The platform on which the entire prototype is built, including the IoT infrastructure and the DT-die, is created by DT. This means that all that was required by the author to implement the full IoT system was to connect the AFE to the DT-die.

B Spice model code listing

B.1 Spice listing for transistor TF412S

The Spice listing for TF412S is fetched from [25].

```
*
*****************************************************
*                   Model of  TF412S                *
*                      package: SOT-883             *
*****************************************************
*                                                   *
*                         J-FET Model               *
*                                                   *
*                EXTERNAL PINS DESCRIPTION          *
*                                                   *
*                     PIN 1 -> SOURCE               *
*                     PIN 2 -> DRAIN                *
*                     PIN 3 -> GATE                 *
*                                                   *
*                  DATE:   Jan.  24,  2014          *
*****************************************************
* MODELLING FOR TF412S

.SUBCKT  TF412SXDFN3  1  2  3
LL3    3  31       0.1n
J1    21  31  11   TF412
LW1   11  12       0.3n
CP1   31  12       0.1p
LL1   12   1       0.1n
LW2   21  22       0.3n
CP2   31  22       0.1p
LL2   22   2       0.1n

.MODEL TF412 NJF(BETA=0.0082 VTO=-0.71 LAMBDA=0.0289
+ RD=97 RS=97 IS=1.10f CGS=3.0p CGD=3.0p M=0.33 PB=0.6
+ FC=0.5 N=1.027 ISR=30f  Nr=2 )

.ENDS TF412SXDFN3
* END OF MODELLING
```

B.2 Spice listing for full system

The Spice listing for the circuitry described in section 9 is given below.

```
* /Users/benedikt/Documents/mo_spice/measurement_circ_test.asc
```

```
Cm V_out 0 5p6
XU1 V_out N001 N003 TF412SXDFN3
V1 N002 0 3.0
XX2 N003 pzt_model
XX1 N002 V_out N001 pulse_gnd_2

* block symbol definitions
.subckt pzt_model V_p
C_p V_p N001 86p
I2 N001 V_p PWL file=/Users/benedikt/Documents/mo_spice/pwls/ltspice_pwl_5p6_1.txt
C1 N001 0 86p
.ends pzt_model

.subckt pulse_gnd_2 vcc_in pulsed_gnd_out vcc_float_duty_out
switch1 vcc_float_duty_out vcc_in N001 0 SW
A1 N001 0 0 0 0 N002 0 0 BUF
switch2 0 pulsed_gnd_out N002 0 SW
V1 N001 0 PULSE(0 1 0 1u 1u 10u 85ms 500)
I1 0 pulsed_gnd_out 1.0715µA
C_ADC pulsed_gnd_out 0 20p
.model sw SW(Ron=0.001 Roff=100Meg Vt=0.5 Vh=.01
.ends pulse_gnd_2

.tran 8 startup
* Sensor element
* DT-die
* TF412S
* Pyroel element
.lib /Users/benedikt/Documents/mo_spice/TF412S-SPICE-D.rev0/TF412S.TXT
.backanno
.end
```

C Substituting the transistor used in the circuit

The traces that surround the components (grey part in figure 28, big copper square in figure 29) are connected to ground. This makes it a challenge to connect a wire to the gate without accidentally connecting it to ground or breaking the brittle pyroelectric element. However, it is possible to remove the lower edge of the copper square and cut straight through the PCB. This does not destroy any traces, as we can see from figure 59. Once this is removed it is possible to solder a wire onto the gate, for instance by using a soldering oven and solder paste, which is less likely to break the pyroelectric element. The result of this is seen in figure 60

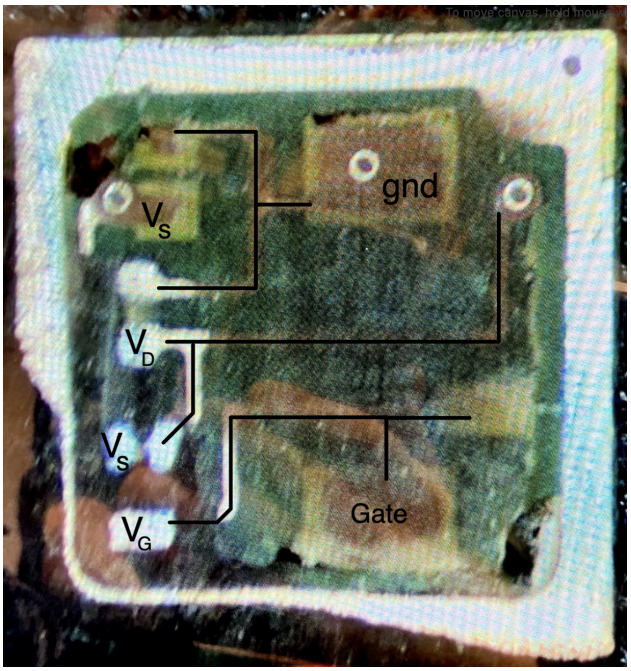

Figure 59: The back side of the sensor after being sanded down. This reveals the traces of the PCB. It is clear that no important traces go along the lower edge below the gate and that this part of the sensor can be safely removed

Once the lower edge has been carefully cut one can use solder paste and a reflow oven to connect a wire to the gate, as shown in figure 60. Then one can connect the gate of the transistor of choice to the wire. Additionally one should remove the existing transistor, $C_{i,1}$, and $C_{i,2}$.

Figure 60: A sensor in which the output port of the pyroelectric element has been made available. Note that it has not been connected to the breadboard, so there is no C_m or transistor in this image.

D Flux of a human passing the sensor element

Figure 61 illustrates a Peltier element placed above a sensor element. We know that the flux from the Peltier element and of a human passing the sensor is the same since they result in the same signal from the sensor element. This means that we can calculate the flux for the particular experiment shown in figure 25 (which shows a person passing below a sensor element).

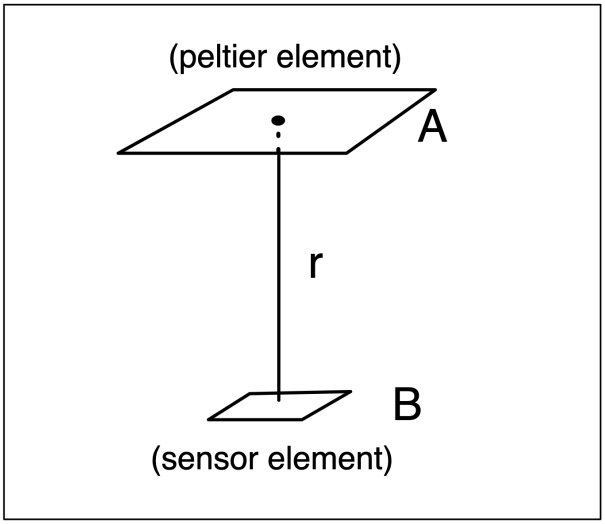

Figure 61: The heat flux received by the sensor element depends on the area of the Peltier element and the distance from it. Area A is the area of the Peltier element. Area B is the area of the sensor. The distance between the sensor and the Peltier element is r. Alternatively, it may illustrate the area of a person (top view) and the sensor element.

The power radiated by the Peltier element is given by the Stefan-Boltzmann law

$$P_{A,out} = \sigma \cdot A_A \cdot T_A^4 \tag{19}$$

where $\sigma \approx 5.67 \cdot \times 10^{-8}$ W m^{-2} K^{-4} is Stefan-Bolzmanns constant, A_A is the area of the Peltier element, and T_A is its temperature. This assumes we approximate it as a black body, otherwise, we would have to multiply with the emissivity ϵ.

The power density at a distance r deteriorates as the inverse of the surface area of a sphere. (inverse square law of radiation).[18] This means that the heat flux $\Phi_{q,r}$ at distance r from element A is given as

$$\Phi_{q,r} = \frac{P_{A,out}}{4\pi r^2} \tag{20}$$

For an element placed at distance r, with area A_B the received power will be

$$P_{B,in} = \Phi_{q,r} \cdot A_B = \left(\frac{\sigma \cdot A_A \cdot T_A^4}{4\pi r^2} \right) \cdot A_B \tag{21}$$

[18] Here we make an approximation of A as a point source.

if one approximates the emissivity of the sensor as one.

E Inaccuracies and approximations in the simulation

E.1 Simulation resolution parameters

If the default resolution of LTspice is used to run the simulation this can result in simulation errors with an amplitude of around 10mV at $V_{out}(n \cdot t_s)$. In order to solve this one can improve the parameters for the simulation.

For the simulations made in the thesis, the simulation parameters in table 3 were used. The integration method used for the simulations is "modified trap". This results in an amplitude of simulation errors at $V_{out}(n \cdot t_s)$ less than 100μV.

gmin	$1E-13$
abstol	$1E-13$
reltol	0
chgtol	$1E-15$
trtol	2
volttol	$1E-06$
sstol	0,001
mindeltagmin	0,0001

Table 3: The values used for LTSpice simulations.

E.2 Numerical inaccuracy in resampling

The Python library called Pandas is what was used for resampling the simulated signal to obtain $V_{out}(n \cdot t_s)$. The precision with which it performs the arithmetic in the resampling function may in some cases lead to inaccuracies such as the ones shown in figure 62.

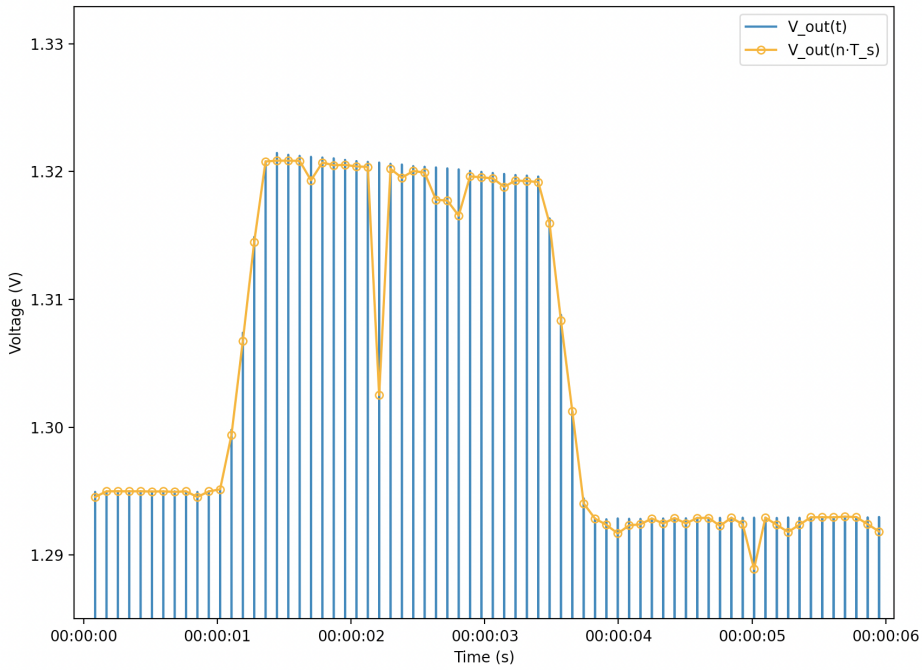

Figure 62: Limited precision in floating point arithmetic may lead to inaccuracies in the resampled signal

The plot of $V_{out}(n \cdot t_s)$ in figure 62 is the exact same as in figure 38 except that the data points that have too low precision have been pruned in figure 38. That is why the sample points (shown as circles) in figure 38 are not entirely evenly spaced.

Figure 63 further illustrates this point.

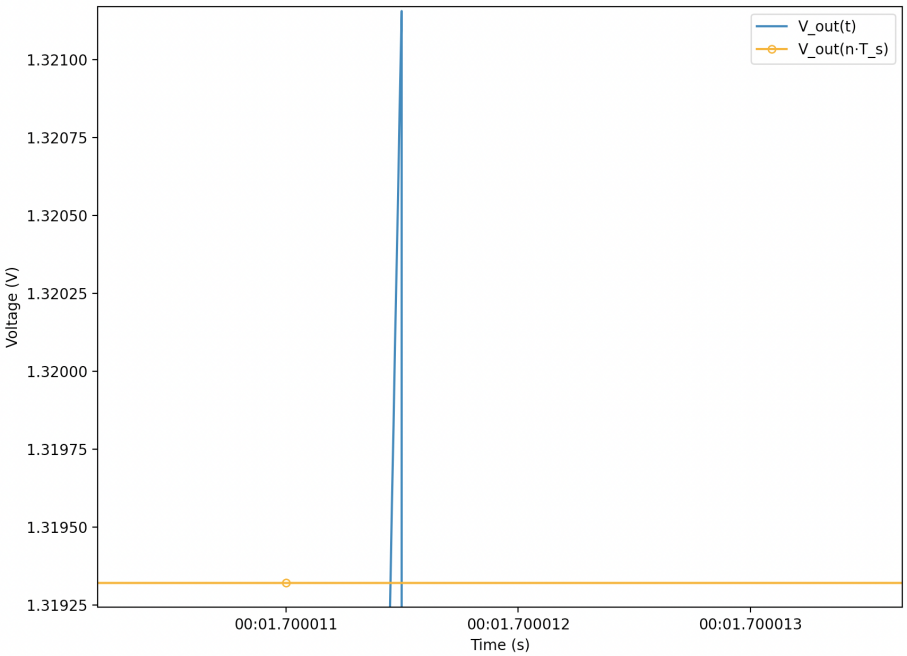

Figure 63: This shows that the internal representation used in pandas may lead to some inaccuracies. $V_{out}(n \cdot t_s)$ is sampled from $V_{out}(t)$ yet the sample can be seen to not be placed on top of $V_{out}(t)$.

An overlay between measured data and simulated data, in which the inaccurate samples have not been pruned can be seen in figure 64.

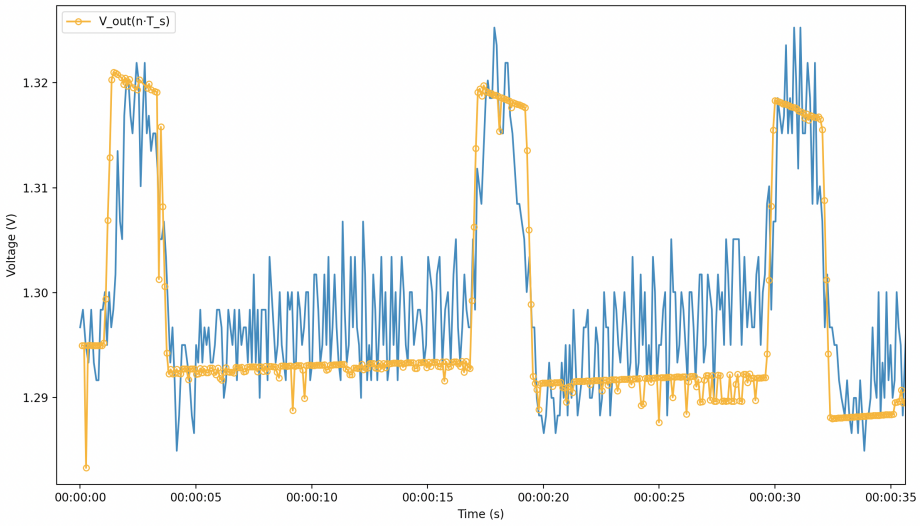

Figure 64: A comparison between simulation and measurement. What looks like noise in the simulation is caused by limited precision in floating point arithmetic during resampling.

E.3 Approximation of pyroelectric current

Figure 65 shows an approximation of the current I_p. It is a PWL (PieceWise Linear) function that one can set as a parameter for I_p in LTspice. Ideally, I_p should be determined by the physical properties of our sensor, as suggested for further work in section 12.4. However, for the purposes of this thesis, the approximation presented here suffices. The approximation is made by finding a current that makes the simulation fit one measurement, and observing that it generalizes well to other measurements.

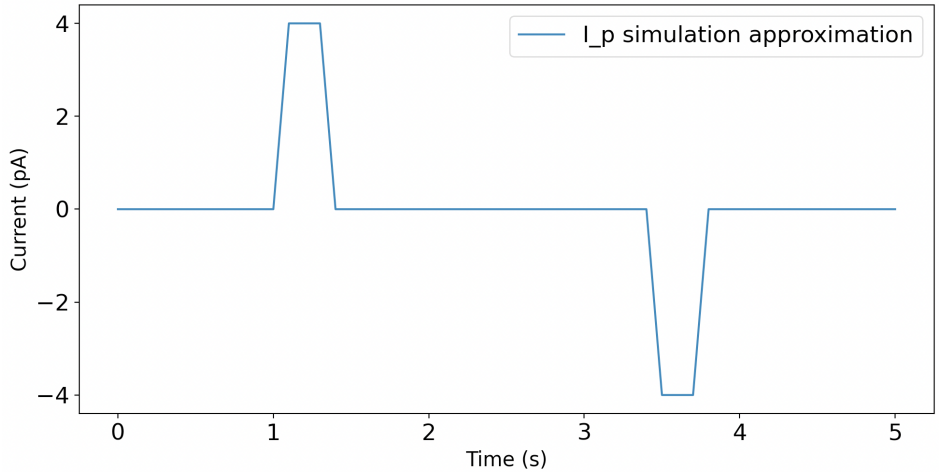

Figure 65: A plot of the approximation for I_p used in the simulation

The expression for I_p used to plot figure 65 is given in table 4.

Time (s)	current (pA)
0	0
1	0
1.1	4
1.3	4
1.4	0
3.4	0
3.5	-4
3.7	-4
3.8	0
5	0

Table 4: The values used for I_p in the simulation.

Figure 66 shows the integral of the current from figure 65. This integral is the charge accumulation from I_p over C_m, which is proportional to V_p and explains the shape that we get for V_p in the simulation.

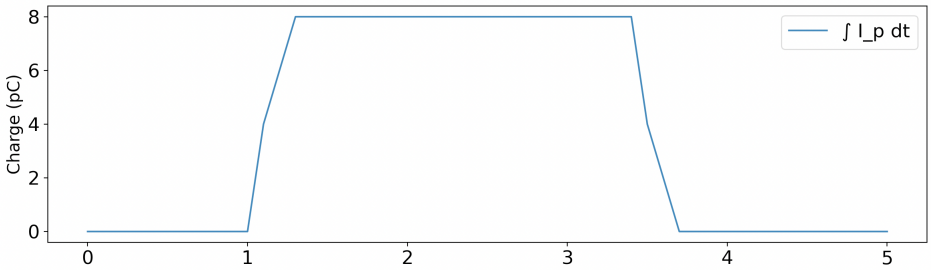

Figure 66: If we take the integral of the current in figure 65 we get this graph of the charge. This should have a similar shape to figure 4.

E.4 Differential pair in simulation

As mentioned in section 3.2 a differential pair is used to get more stable measurements. The equivalent model for this differential pair may be seen in figure 67.

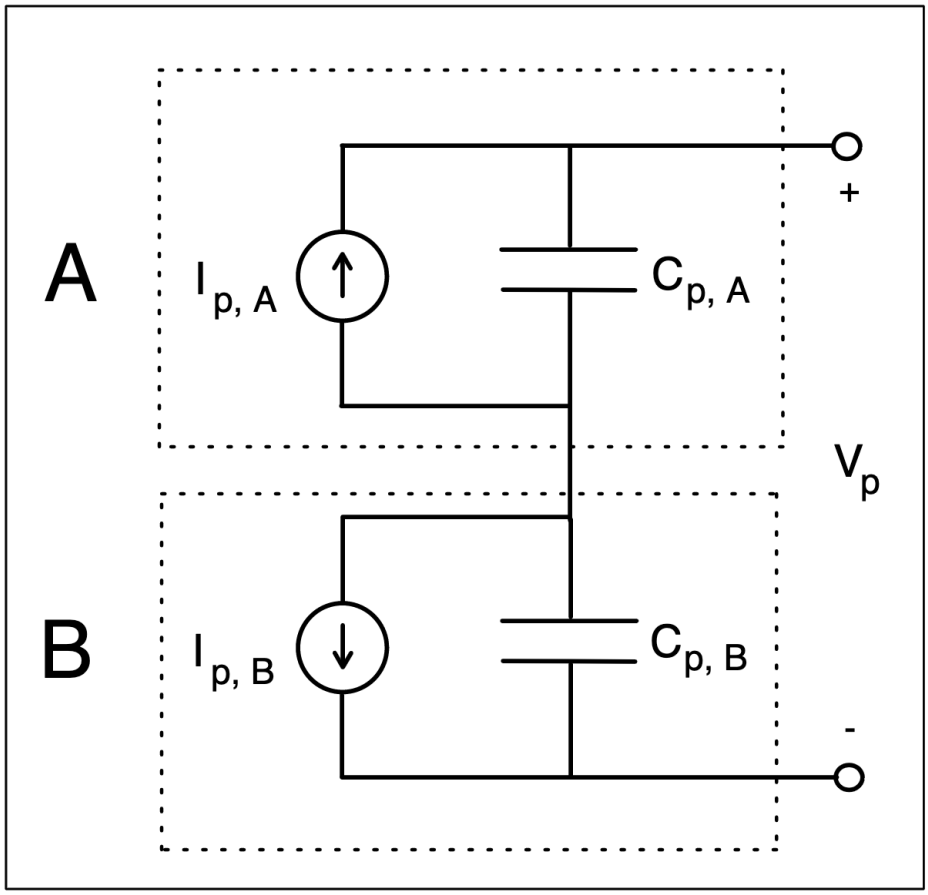

Figure 67

However, we can consider $I_{p,B}$ to be zero because it is obscured by the "lid", and does not experience the rapid temperature changes from a person passing the sensor. The only change from the other simulations in the thesis is that we have $I_{p,A} = 2I_p$ and $C_{p,A} = C_{p,B} = 2C_p$. With these values, all the simulation results will be the same as in the rest of the thesis. The logic behind this is that $C_{p,A}$ in series with $C_{p,B}$ with these

values results in a total capacitance equal to C_p. When the current $I_{p,A}$ charges a capacitor that is twice as big, twice the current is required to achieve the same voltage.

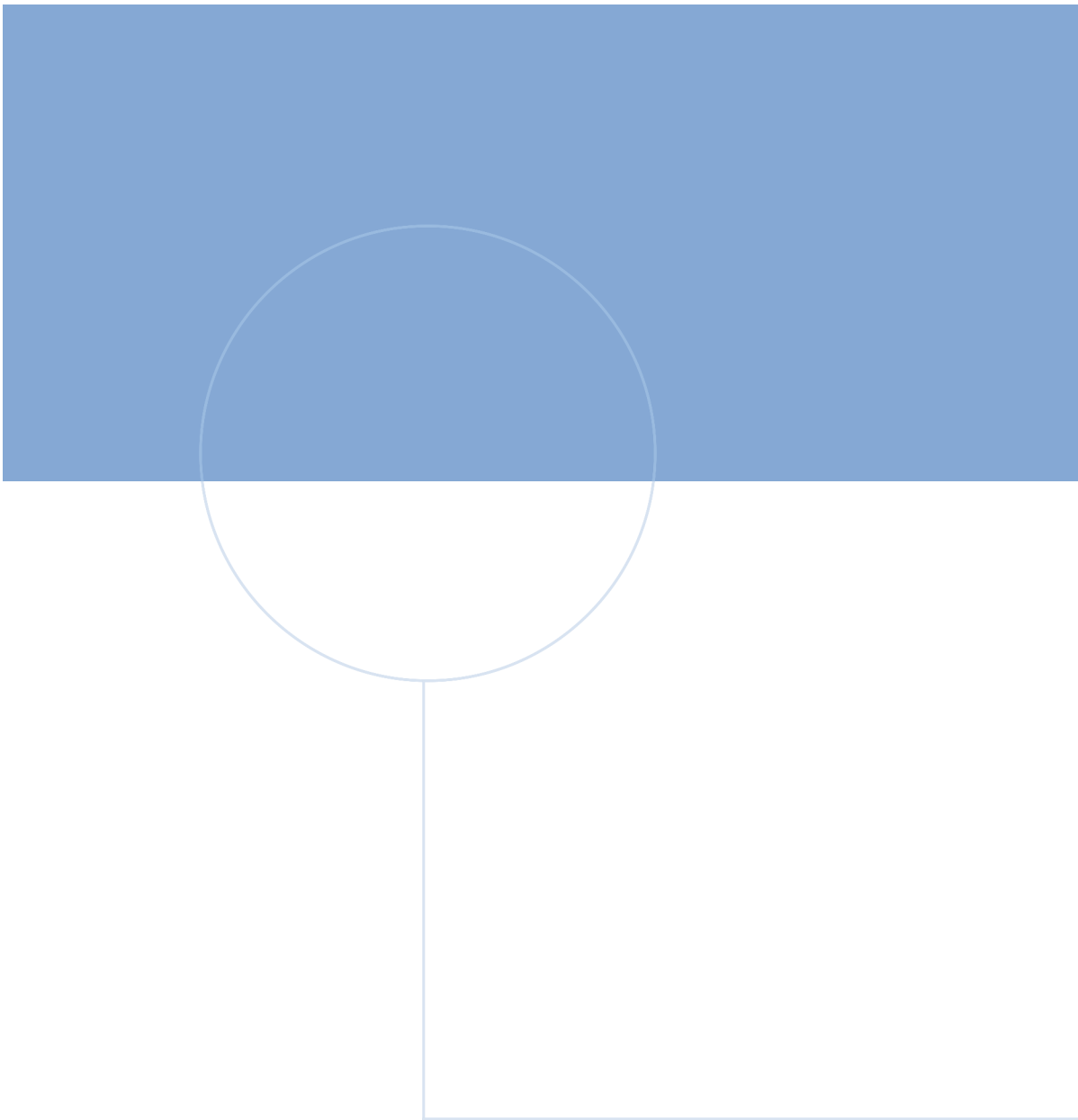

NTNU

Norwegian University of
Science and Technology